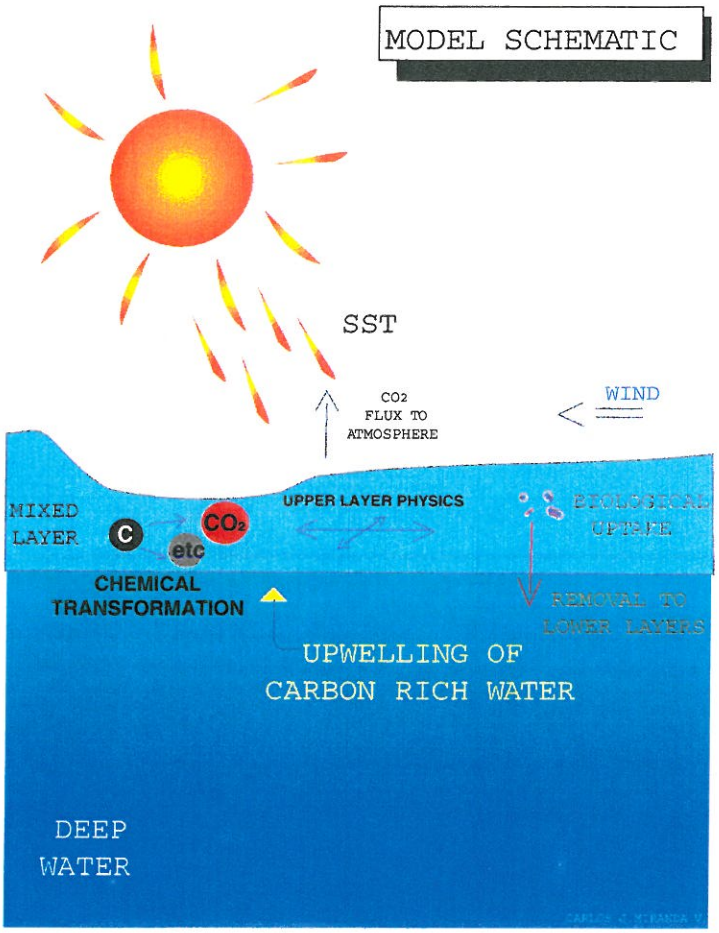
CENTER FOR OCEAN-ATMOSPHERIC PREDICTION STUDIES
THE FLORIDA STATE UNIVERSITY
TALLAHASSEE, FL 32306-3041, USA
DIRECTOR: DR. JAMES J. O'BRIEN

MECHANISMS OF INTERANNUAL CO_2 FLUX VARIABILITY IN THE EQUATORIAL PACIFIC OCEAN

By

MARK ALAN VERSCHELL



DECEMBER 1996
TECHNICAL REPORT 96-5

TABLE OF CONTENTS

FOREWORD iii

ABSTRACT v

1. Introduction 1

2. Model 11
   2.1 Hydrodynamic ocean model 11
   2.2 Biogeochemical model 14

3. Experiments 17

4. Results 19
   4.1 Climatology 19
   4.2 Results of basic model run 21
   4.3 Model comparisons 24

5. Comparison With Observational Data 47
   5.1 Ocean carbon measurements 47
   5.2 Oceanic proxy measurements 50
   5.3 Atmospheric proxy measurements 53

6. Discussion 59

APPENDICES 67

A. Derivation of Biogeochemical model 67

B. Computation of pCO_2 in seawater 71

ACKNOWLEDGEMENTS 75

REFERENCES 77

FOREWORD

COAPS scientists and students have studied the equatorial Pacific since 1975. The "FSU Winds" are famous and are used by almost everyone who has need for wind data in the tropical Pacific. Currently they are available from 1930 to November 1996. Besides El Niño and El Viejo, the equatorial Pacific Ocean is unique since it "belches" copious quantities of CO_2 into the atmosphere, usually more than 1 gigaton of carbon per year.

This is the Ph.D. dissertation of Mark Verschell. It explains how the physics of the tropical ocean and atmosphere regulate the CO_2 flux to the atmosphere. A unique part of this work is the use of more than 100 million actual observations of wind and sea surface temperature which are incorporated into the model to achieve fidelity. And each datum was measured by a human being.

In this biogeochemical model, we finesse the biology. If the reader wants more biology please tell me why. The geochemistry of dissolved carbon to PCO_2 is very complicated. In this work, Verschell shows how to compress this very interesting and complex chemistry into a table lookup.

It will be a surprise to many that the physical oceanographic processes dominate the reasons for the variability. The divergence of surface currents creates the vertical transport of nutrients and the variable wind stress modulates the bulk of the air-sea transfer.

In fact the world is much simpler than one is lead to believe. Have fun reading and send us your critique.

James J. O'Brien
Director, COAPS
Distinguished Research Professor
Meteorology and Oceanography

ABSTRACT

A high-resolution biogeochemical model is developed to examine the flux of carbon dioxide from the equatorial Pacific Ocean, the major oceanic source of atmospheric carbon. The model is run for the thirty year period from 1965 to 1994 to investigate interannual variability in the carbon dioxide flux and the mechanisms leading to this variability. The model is forced by upper layer velocities and upwelling from a non-linear high-resolution hydrodynamical model of the tropical Pacific Ocean, the Florida State University Wind Stresses, and the Reynolds sea surface temperatures. The two data sets consist of tens of millions of individual real world observations.

The model demonstrates the link between the interannual variations of the carbon dioxide flux and the El Niño/Southern Oscillation (ENSO), and identifies the responsible mechanisms. In particular, ENSO warm events are associated with decreased carbon dioxide flux because of the reduced upwelling of deep, carbon rich water into the surface layer and the weakening of the equatorial trade winds that drive the flux. In contrast, during ENSO cold events enhanced upwelling of deep, carbon rich water and stronger trade winds cause increased carbon dioxide flux from the equatorial Pacific Ocean. Carbon dioxide flux from the biogeochemical model compares well with the limited long-term observational data available. Interannual variations of the flux and proxy ENSO indices of sea surface temperature and thermocline depth also indicate good agreement.

Replacing one input forcing field of either upper layer velocities and upwelling, wind stresses, or sea surface temperatures with six-day climatologies of

the respective field indicates that both winds and upper layer physics are essential to reproduce the interannual flux variability. Sea surface temperature is less important in determining the variability. Results from a box model forced by zonally averaged input fields demonstrates that modeling the carbon dioxide flux from the equatorial Pacific requires an accurate representation of the critical horizontal spatial scales in the region.

1. Introduction

Studies of atmospheric CO_2 variability date to the early 19th century when *de Saussure* [1830] carried out systematic measurements of regional CO_2 concentrations. Since this early research, there has been continuous interest in examining the variability of CO_2 concentration on scales ranging from daily to interannual to millennial. Beginning in 1958 continuous measurements of atmospheric CO_2 have been made from the Mauna Loa Observatory in Hawaii. More recently, measurements of atmospheric CO_2 have become available from the over 100 land and ocean sites under the coordination of the World Meteorological Organization (WMO). As far back as the late 1950's the ocean's role in atmospheric CO_2 concentration has been investigated [e.g., *Craig*, 1957; *Keeling*, 1958; *Broecker and Olson*, 1960].

One major concern is the observed increase in atmospheric CO_2 concentration over the last 150 years and its potential connection to global warming. Researchers attribute this increase mainly to fossil-fuel consumption. Since the beginning of the industrial revolution, the concentration of CO_2 in the atmosphere has been increasing exponentially (figure 1). However, this increase in concentration accounts for less than half the estimated anthropogenic input [*Schimel et al.*, 1994]. The fate of the remaining CO_2 is a matter of great debate [e.g., *Francey et al.*, 1995; *Ciais et al.*, 1995; *Toggweiler*, 1995]. There are two candidates for the so called "CO_2 Sink": the oceans and the terrestrial biosphere. However, the percentage of carbon taken up by each sink is uncertain.

The exponential increase is the most prominent feature of the atmospheric CO_2 time series. In addition, the concentration of atmospheric CO_2 varies

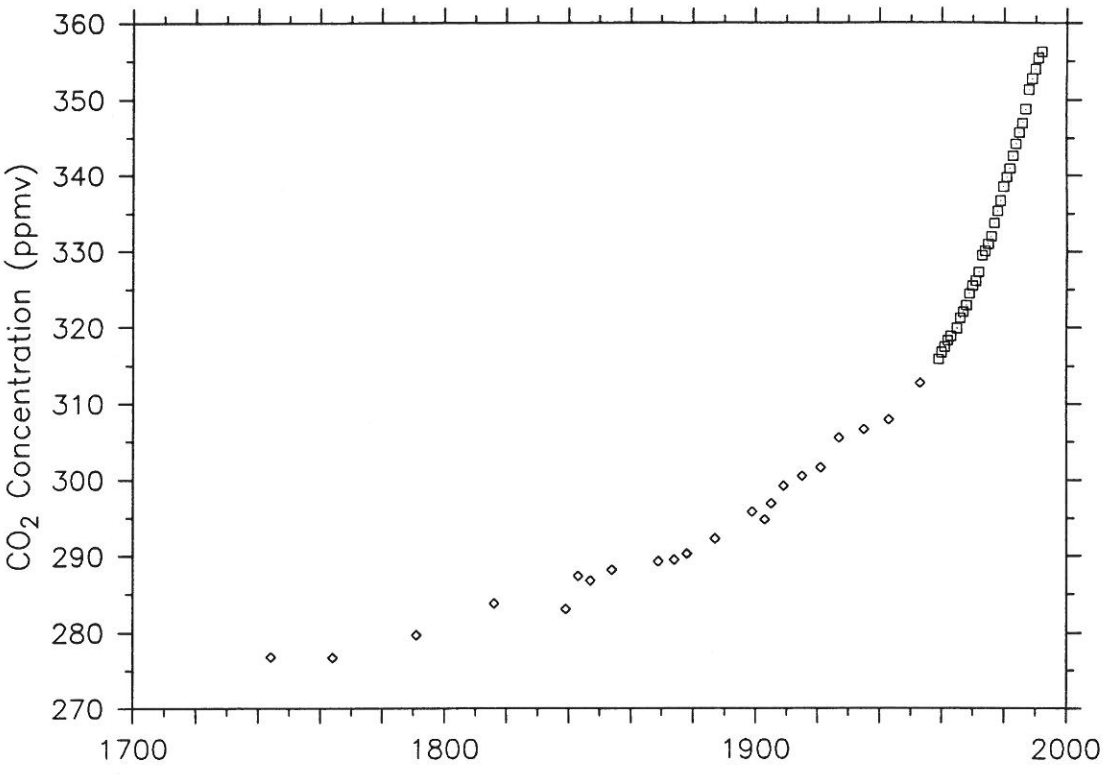


Figure 1: Atmospheric CO_2 concentrations since 1744. Measurements are from air bubbles trapped in ice cores (diamonds) [*Neftel et al.*, 1994], and from Mauna Loa Observatory, Hawaii (squares) [*Keeling and Whorf*, 1994].

on seasonal, annual, and interannual time scales (figures 2 – 3). While some studies have primarily attributed seasonal and annual variations to the uptake and release of CO_2 by the terrestrial biota [*Keeling et al.*, 1989], other studies have linked variability on these time scales to oceanic processes [*Merlivat et al.*, 1991; *Nefedova and Tarko*, 1995; *Antoine and Morel*, 1995; *Taylor*, 1995].

The variability of atmospheric CO_2 concentration on interannual time scales has also been an area of intense study. The debate surrounding interannual variability is the same as that for the "CO_2 sink" and for seasonal and annual

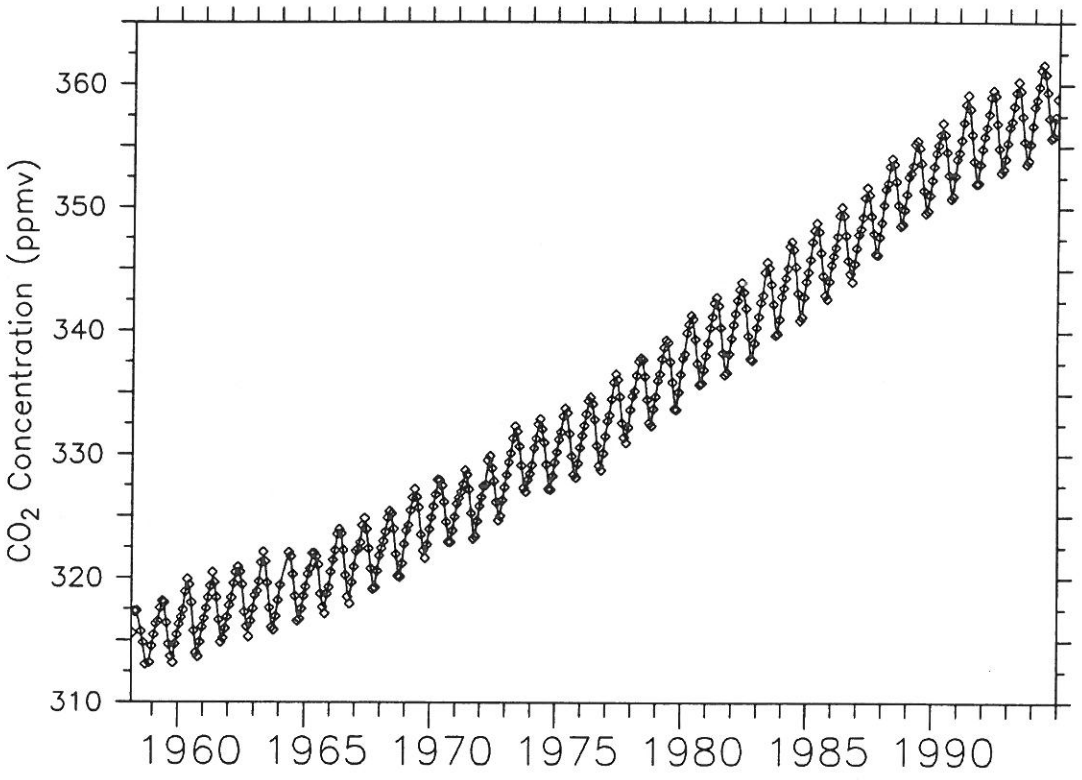


Figure 2: Monthly average CO_2 concentrations from the Mauna Loa Observatory, Hawaii (diamonds), and seasonally smoothed values (solid line). From *Keeling and Whorf* [1994].

variability. Namely, how much influence on the interannual variability is due to terrestrial sources and how much variability is due to oceanic sources [e.g., *Keeling et al.*, 1989; *Martín et al.*, 1994; *Winguth et al.*, 1994; *Meyers and O'Brien*, 1995]. This study focuses on increasing the understanding of the ocean's role in the interannual variability of atmospheric CO_2 concentration.

The oceans have large regions of either net ocean-to-atmosphere CO_2 flux or net atmosphere-to-ocean CO_2 absorption (figure 4; *Takahashi* [1989]). The equatorial regions of the Atlantic, Indian, and Pacific Oceans, as well as the northern Indian and Pacific Oceans are all areas of net ocean-to-atmosphere CO_2 flux.

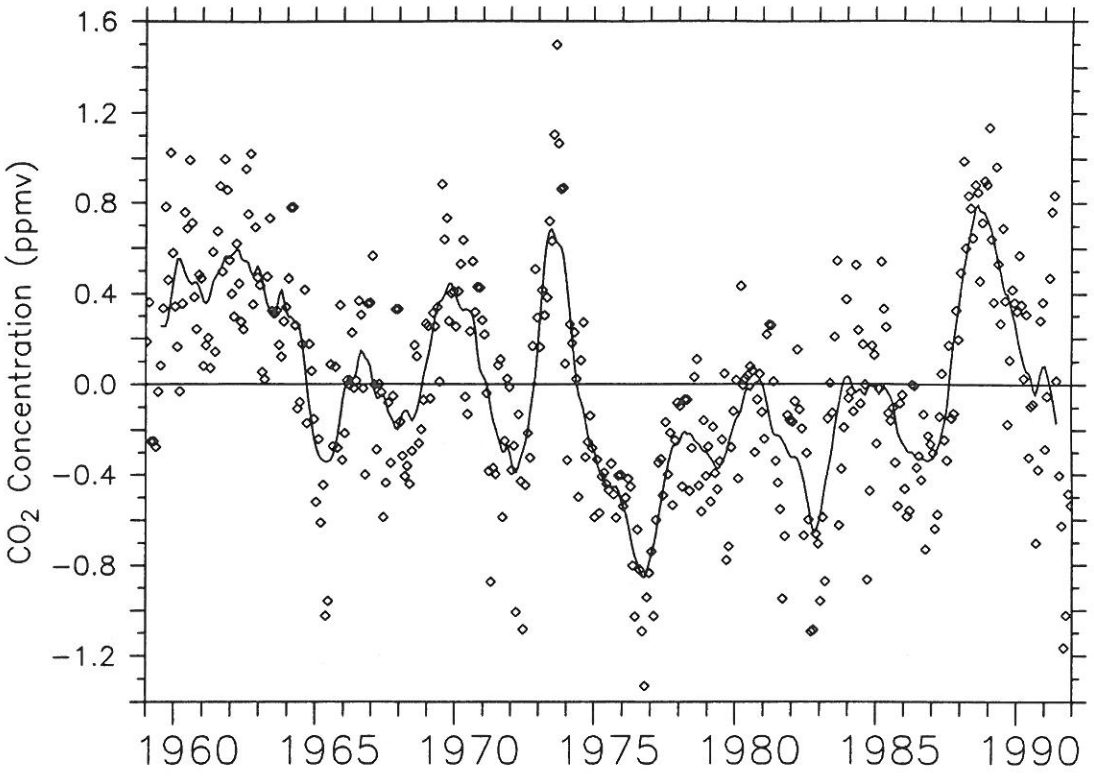


Figure 3: Monthly average CO_2 concentration anomalies from the Mauna Loa Observatory, Hawaii (diamonds), and annually smoothed anomaly (solid line). The monthly average CO_2 concentrations from the Mauna Loa Observatory have been seasonally adjusted and the contribution of CO_2 owing to estimated fossil fuel combustion has been removed. From S. D. Meyers (personal communication).

The southern oceans, the Arctic ocean, and the north Atlantic Ocean are all areas of net atmosphere-to-ocean CO_2 flux. There is an estimated mean annual ocean-to-atmosphere CO_2 flux of 1.55 $Gt-C\,yr^{-1}$ and an estimated mean annual atmosphere-to-ocean CO_2 flux of 3.35 $Gt-C\,yr^{-1}$. On balance, it is estimated that the oceans absorb 1.8 $Gt-C\,yr^{-1}$.

The equatorial Pacific Ocean is the single largest source region of ocean-to-atmosphere CO_2 flux, accounting for over 60% of the mean annual net transfer of CO_2 from the surface waters of the world's ocean [*Libes*, 1992]. The equato-

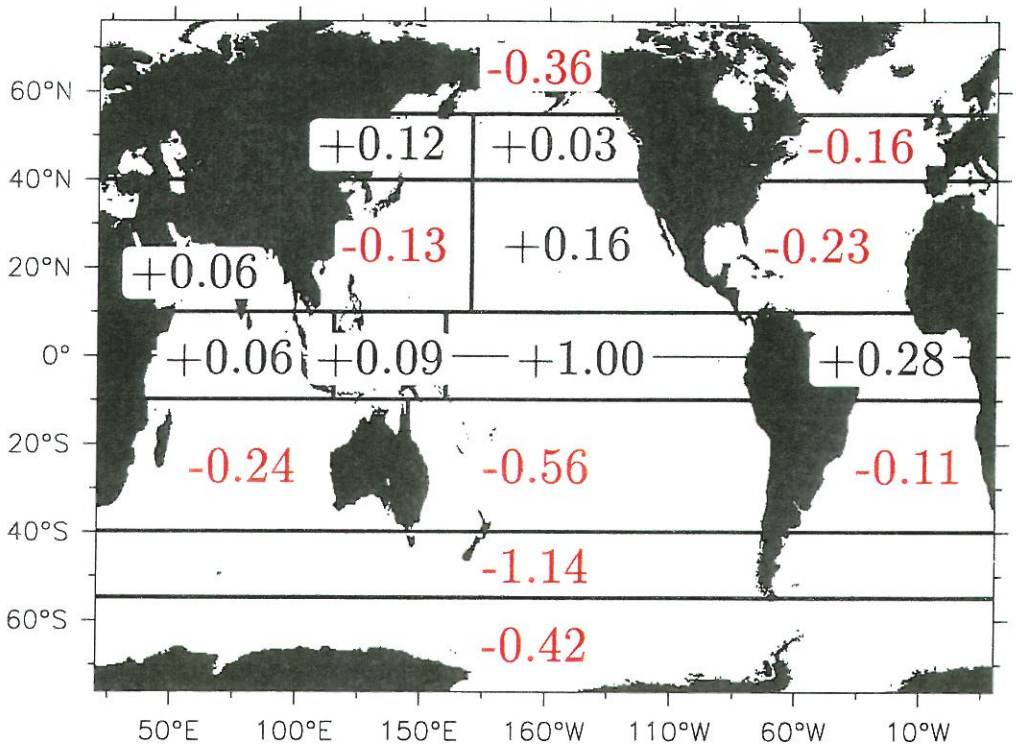


Figure 4: Estimate of mean annual net CO_2 transfer ($Gt-C\ yr^{-1}$) from the ocean to the atmosphere. The equatorial Pacific Ocean is the largest oceanic source of CO_2, accounting for over 60% of ocean to atmosphere CO_2 flux. Adapted from *Takahashi* [1989].

rial Pacific is also the area with the most prominent interannual signal, the El Niño/Southern Oscillation (ENSO). ENSO is associated with large changes in equatorial meteorological and oceanographic quantities, e.g., sea surface temperature (SST), equatorial trade winds, precipitation, and equatorial upwelling. Consequently, the equatorial Pacific provides a logical starting point in the investigation of the interannual variability of ocean-to-atmosphere CO_2 flux.

Many researchers have collected carbon data in the equatorial Pacific Ocean around ENSO warm and cold events. *Feely et al.* [1987] collected data during

and after the 1982-83 ENSO warm event. They determined that decreased upwelling during the warm event had two effects: first, the partial pressure of CO_2 (pCO_2) was reduced to a level that was near saturation with respect to the atmosphere, and second, the ocean-to-atmosphere CO_2 flux became negligible. Further, at the conclusion of the warm event, upwelling resumed, pCO_2 returned to a condition of being highly supersaturated, and a strong ocean-to-atmosphere CO_2 flux was reestablished.

Inoue and Sugimura [1992] took measurements in the equatorial Pacific of pCO_2 from background air and seawater between January, 1987 and February, 1989, a period that included one ENSO warm event (1986/87) and one ENSO cold event (1988/89). They found that there was decreased ocean-to-atmosphere CO_2 flux (Q_{CO_2}) during the warm event ($\approx$ 0.4 $Gt-C\,yr^{-1}$), enhanced Q_{CO_2} during the cold event ($\approx$ 1.0 $Gt-C\,yr^{-1}$), and that the zonal distribution of pCO_2 in the surface waters during this period could be accounted for by the effects on pCO_2 of temperature, salinity, biological activity and CO_2 flux to the atmosphere. They hypothesized that this large interannual variation could effect the growth rate of atmospheric CO_2. Moreover, they believe that the long-term trend in the ^{13}C component ($\delta^{13}C$) of atmospheric CO_2 concentration indicates enhanced releases of CO_2 from the terrestrial biosphere between 1987 and 1988, and enhanced releases of oceanic CO_2 during the period 1988 to 1989.

Feely et al. [1995] took measurements of atmospheric and oceanic pCO_2 in the central and eastern equatorial Pacific during the northern spring and autumn of 1992, an ENSO warm event period. They estimated that there was a net annual reduction of Q_{CO_2} to the atmosphere of about (0.5-0.7 $Gt-C\,yr^{-1}$).

Wanninkhof et al. [1996] collected surface water CO_2 fugacities (fCO_{2w}, partial pressure of a non-ideal gas), Q_{CO_2}, and SST measurements along 5 transects in the central and eastern equatorial Pacific during the anomalously warm period in the eastern equatorial Pacific (called the 1992-93 ENSO warm event by some researchers). fCO_{2w} takes into account the nonideality of CO_2, and typically differs from pCO_2 by 0.5 to 1.5 μatm in surface waters. When compared with similar data obtained during the spring of 1986 and the spring of 1989, they found large interannual variabilities in the location and magnitude of the fCO_{2w} maxima. They hypothesized that this variability is the result of the existence of two different mechanisms for the formation of fCO_{2w} maxima, one for regions of low SST and one for regions of high SST. In regions where SST is low, fCO_{2w} maxima occur when water with high carbon content is being upwelled (low SSTs in the equatorial region are an indicator of strong upwelling). In regions where SST is high, maxima occur when the fCO_{2w} created by local heating outpaces the decreases in fCO_{2w} caused by export production and gas exchange.

Several modeling studies have looked at either the steady-state condition of CO_2 flux from the equatorial Pacific or the changes in the equatorial CO_2 flux associated with individual ENSO events. *Volk and Liu* [1988] made an early attempt to examine the connection between the equatorial Pacific and anomalous Q_{CO_2} using a three surface ocean box model. They determined that outgassing in this region is controlled mainly by temperature, with higher temperatures corresponding to larger CO_2 flux. *Volk* [1989], using a descendant of his earlier box model, showed a connection between the cessation of upwelling during an ENSO warm event and the decrease in pCO_2 in equatorial Pacific

surface waters 1 to 2 months later. This result is supported by *Meyers and O'Brien* [1995].

Maier-Reimer [1993], using a coarse resolution general circulation model (GCM) coupled to a geochemical tracer model of the Michaelis-Menten type, was able to reproduce a realistic global tracer distribution. The model's coarse resolution, however, resulted in equatorial Pacific upwelling that was significantly exaggerated, leading to unrealistic results. *Winguth et al.* [1994] using the same GCM as *Maier-Reimer* [1993] coupled to an oceanic carbon cycle model (HAMOCC-3) investigated the connection of the 1982/1983 ENSO to Q_{CO_2}. They showed that the cessation of equatorial upwelling during the 1982/83 ENSO warm event lead to an anomalously low ocean-to-atmosphere CO_2 flux. These results supported the earlier research of *Volk* [1989] and *Keeling et al.* [1989] (described above) as well as other studies [e.g., *Keeling and Revelle*, 1985; *Winguth*, 1992].

A few researchers have studied long term oceanic interannual variability and its connection to atmospheric variability. *Martín et al.* [1994] found that SST anomalies in the eastern equatorial Pacific Ocean preceded changes in the growth rate of atmospheric CO_2 at Mauna Loa by about 5 to 7 months. These SST anomalies also preceded changes occurring at Samoa and the South Pole by 7 to 9 months, and changes occurring at Barrow (Alaska) by 8 to 13 months. However, they found inconsistencies in this pattern and concluded that the ocean, or at least oceanic SST anomalies, cannot completely account for atmospheric CO_2 anomalies. *Meyers and O'Brien* [1995] redefined the onset and duration of ENSO based on sea level anomalies at central equatorial Pacific

islands. Using this definition they found that ENSO warm and cold events lead corresponding negative and positive CO_2 anomalies by 1 to 2 months with a maximum correlation of 0.47. These results suggest that the central equatorial Pacific is the source of most of the atmospheric CO_2 flux variations.

On the other hand, no long-term modeling or observational studies of the interannual variability of CO_2 flux from the equatorial Pacific Ocean have been reported in the literature. The existing research involves either long-term forecast models describing the ocean's response to atmospheric CO_2 increases [e.g., *Klepper et al.*, 1994; *Klepper and de Haan*, 1995; *Keller and Goldstein*, 1995; *Tett*, 1995], or steady-state dynamic models forced by various chemical perturbations [e.g., *Toggweiler et al.*, b1989b; *Sarmiento et al.*, 1992].

This study is the first attempt to model the interannual variability of the CO_2 flux from the equatorial Pacific Ocean, and to determine the mechanisms leading to this variability. In order to accomplish this, a high resolution biogeochemical CO_2 flux model of the equatorial Pacific Ocean is coupled to a non-linear hydrodynamic model of the tropical Pacific. The model is forced by the Florida State University wind stresses and the Reynolds SSTs (comprising tens of millions of individual real world observations). Various experiments are run to examine the interannual variability of the CO_2 flux and the physics causing this variability.

This research is presented in five sections. First, the model used in this work is described. This model consists of two components that are run separately: (1) a hydrodynamic model of the upper tropical Pacific Ocean and (2) a biogeochemical model of the equatorial Pacific Ocean. Second, the various

experiments designed to investigate the physics of the interannual variability in CO_2 flux from the equatorial region are detailed. Third, the results of the experiments are presented. Fourth, comparisons are made between oceanic and atmospheric data. Lastly, the results of the model runs and the comparisons with observational data are discussed.

It will be demonstrated that an accurate representation of both the upper layer dynamics and the overlaying wind field are required to determine the CO_2 flux from the equatorial Pacific Ocean. Box models, steady-state experiments, and low-resolution finite-difference models cannot adequately reproduce the CO_2 flux from this region. Further, it will be shown that most of the CO_2 flux as well as the variability in this CO_2 flux originates from the central equatorial Pacific, not the eastern equatorial Pacific as previously thought [e.g., *Winguth et al.*, 1994; *Martín et al.*, 1994; *Keeling et al.*, 1995].

Finally, this study will show that the ocean-to-atmosphere CO_2 flux is highly influenced by interannual variability in the equatorial Pacific. During an ENSO warm event CO_2 flux is greatly reduced as a result of: (1) the deepening of the thermocline which reduces the normally strong equatorial upwelling, and (2) the weakening of the easterly trades. By the same token, during an ENSO cold event, stronger upwelling and easterly trades enhance CO_2 flux. SST is not a primary effect influencing the interannual variability of CO_2 flux.

2. Model

The model used in this study has two components which are run independently of each other. The first component is a $1\frac{1}{2}$ layer reduced gravity ocean model of the tropical Pacific forced by realistic monthly mean winds. This component contains all of the essential upper ocean hydrodynamics. The second component is an equatorial Pacific biogeochemical carbon tracer conservation model which is used to calculate the oceanic pCO_2 and the corresponding flux of CO_2 to the atmosphere (Q_{CO_2}). Figure 5 shows the geometry of the study region, and the domain of the model components.

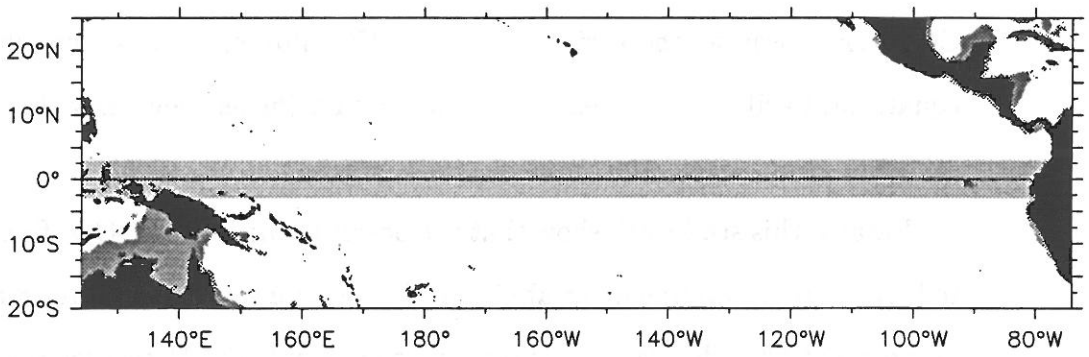


Figure 5: Detail of study region. The hydrodynamic model is integrated over the entire region shown. The light grey box denotes the domain of the biogeochemical model.

2.1 Hydrodynamic ocean model

The hydrodynamic ocean model used in this experiment is a reduced gravity, nonlinear shallow water transport model of the tropical Pacific Ocean. The description here will be brief. A complete discussion of the model can be found in *Kamachi and O'Brien* [1995]. The model is formulated in spherical coordinates

on an Arakawa C grid. The equations of motion for this model (with ϕ being longitude and θ being latitude) are

$$\frac{\partial U}{\partial t} + \frac{1}{a\cos\theta}\frac{\partial}{\partial\phi}\left(\frac{U^2}{h}\right) + \frac{1}{a}\frac{\partial}{\partial\theta}\left(\frac{UV}{h}\right) - (2\Omega\sin\theta)V$$
$$+ \frac{g'h}{a\cos\theta}\frac{\partial h}{\partial\phi} - \frac{\tau^{(\phi)}}{\rho} - \frac{A}{a^2\cos^2\theta}\left[\frac{\partial^2}{\partial\phi^2} + \cos\theta\frac{\partial}{\partial\theta}\left(\cos\theta\frac{\partial}{\partial\theta}\right)\right]U = 0, \quad (1)$$

$$\frac{\partial V}{\partial t} + \frac{1}{a\cos\theta}\frac{\partial}{\partial\phi}\left(\frac{UV}{h}\right) + \frac{1}{a}\frac{\partial}{\partial\theta}\left(\frac{V^2}{h}\right) + (2\Omega\sin\theta)U$$
$$+ \frac{g'h}{a}\frac{\partial h}{\partial\theta} - \frac{\tau^{(\theta)}}{\rho} - \frac{A}{a^2\cos^2\theta}\left[\frac{\partial^2}{\partial\phi^2} + \cos\theta\frac{\partial}{\partial\theta}\left(\cos\theta\frac{\partial}{\partial\theta}\right)\right]V = 0, \quad (2)$$

$$\frac{\partial h}{\partial t} + \frac{1}{a\cos\theta}\left[\frac{\partial U}{\partial\phi} + \frac{\partial}{\partial\theta}(V\cos\theta)\right] = 0, \quad (3)$$

where $U = uh$ and $V = vh$, represent the eastward and northward components of the upper layer transport; (u, v) are the depth independent eastward and northward upper layer vector velocity components; h is the upper layer thickness; a is the equatorial radius of the Earth; Ω is the Earth's angular velocity; $g' = g(\Delta\rho/\rho)$ is the reduced gravity constant; $(\tau^{(\phi)}, \tau^{(\theta)})$ are the eastward and northward wind stress components modeled as a body force acting over the entire layer depth; ρ is the horizontally constant upper layer density; A is the horizontal eddy viscosity; g is the gravitational acceleration; and $\Delta\rho$ is the density difference between the active upper layer and the infinitely deep, quiescent lower layer.

Equations (1)–(3) are integrated numerically on a sphere in the region 124°E to 74°W and from 20°S to 25°N (figure 6). The horizontal resolution is 0.25° in both longitude and latitude, between like variables. The model basin uses realistic coastline geometry including major islands, with a no-slip boundary condition applied. The model is integrated in time using a leapfrog scheme with a forward difference scheme being used every 77th time step to eliminate the computational mode (an artifact of the time differencing scheme). The diffusive terms are computed using a DuFort-Frankel scheme. An open boundary condition of the type described in *Camerlengo and O'Brien* [1980] is applied to the northern and southern boundaries of the model region. In addition, a mass entrainment scheme prevents layer surfacing, and mass conservation is applied every 48 time steps to offset mass flux through the open boundaries. The parameters used in the hydrodynamic model are set out in Table 1.

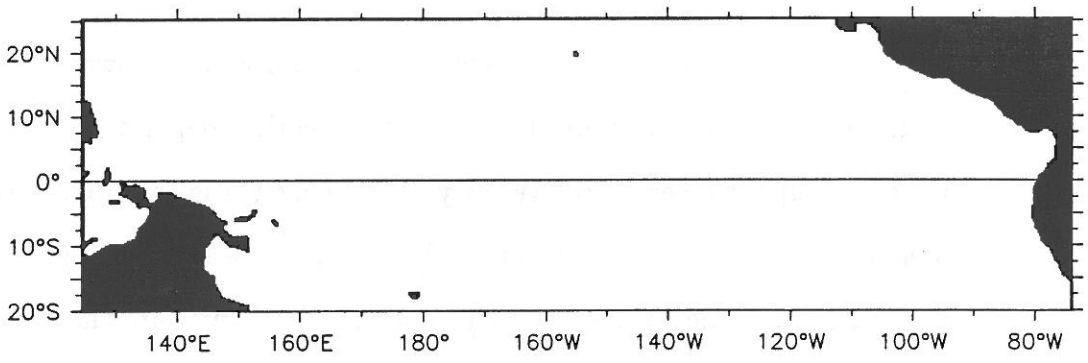


Figure 6: Detail of geometry for hydrodynamical tropical Pacific Ocean model.

Table 1: Parameters used in hydrodynamic ocean model.

Parameter	Value
δt	30 minutes
A	750 m^2 s^{-1}
g'	0.02 m s^{-2}
ρ	1025.0 kg m^{-3}
H	300 m
$H_{\min}$	80 m
ρ_{air}	1.2 kg m^{-3}
C_D	0.0017

2.2 Biogeochemical model

The biogeochemical model developed for this study is an equatorial carbon tracer model. The basic form of the tracer conservation equation is

$$\frac{\partial C}{\partial t} + \nabla \cdot C\mathbf{u} + \frac{\partial Cw}{\partial z} = S. \tag{4}$$

where C is CO_2 concentration and S (sources minus sinks) includes not only chemical and biological transformations but also CO_2 flux to the atmosphere.

Equation 4 is first integrated over a constant mixed layer thickness, H, and then Reynolds averaged (spatial) from 3°S to 3°N. After making the eddy diffusivity assumption [*von Schwind*, 1980] we obtain

$$\frac{\partial \bar{C}}{\partial t} + \frac{\partial \bar{C}\bar{u}}{\partial x} + K\frac{\partial^2 \bar{C}}{\partial x^2} = \bar{S} - \bar{C}_{-H}\bar{w}_{-H} - \frac{Cv}{L}\Big|_S^N \tag{5}$$

where

$$\bar{()} = \int_{-3^\circ}^{+3^\circ} ()dy$$

u = upper layer zonal velocity

v = upper layer meridional velocity

L = distance between 3°S and 3°N

K = Eddy diffusivity constant

The $\bar{S}$ term includes CO_2 flux from the ocean to the atmosphere, chemical transformation, and biological activity. A complete derivation of the biogeochemical model can be found in Appendix A.

CO_2 flux to the atmosphere is calculated using a version of the formulation of *Wanninkhof* [1992]

$$Q_{CO_2} = \left[2.5\left(0.5246 + 1.6256 \times 10^{-2}T + 4.9946 \times 10^{-4}T^2\right) + 0.3\tau^2\right]\left(\frac{660}{Sc}\right)^{1/2} \Delta pCO_2, \quad (6)$$

where τ is the wind speed at 10m; T is the Reynolds SST [*Smith et al.*, 1996]; Sc is the temperature and salinity dependent diffusion coefficient (Schmidt number); and ΔpCO_2 is the difference between the oceanic and atmospheric pCO_2 (chosen to be 0.15 the oceanic pCO_2). It is assumed that any equatorial uptake of CO_2 is small, therefore Q_{CO_2} is always greater than or equal to 0. The ΔpCO_2 is chosen to be a fraction of the oceanic pCO_2 to reflect that the vertical profile of pCO_2 is not a step function between the pCO_2 of the ocean and the pCO_2 of the atmosphere, but rather a gradient between the two. Since the atmospheric pCO_2 is relatively constant on an interannual time scale while the oceanic pCO_2 is not, the approximation that ΔpCO_2 is dependent only on the oceanic pCO_2

is made.

Equation 6 is linearized about a mean salinity of 34.551‰, and then Taylor series expanded about a mean SST of 27.134°C and a mean squared wind speed of 4.79 $m^2\ s^{-2}$, giving

$$Q_{CO_2} = (4.4 \times 10^{-8} + 9.4 \times 10^{-9}T + 2.7 \times 10^{-8}\tau^2)\Delta pCO_2. \qquad (7)$$

pCO_2 is a complicated function of CO_2 relating to temperature, salinity, alkalinity, and the total concentrations of dissolved CO_2, silica, borates, and phosphate. pCO_2 is calculated with a method based on *Broecker and Takahashi* [1978] (see Appendix B).

The biological component of $\bar{S}$ is a function of upwelled nitrate (the limiting nutrient), and the extraction of available carbon in an amount proportional to the Redfield ratio.

Parameters used in the biogeochemical model are set out in Table 2.

Table 2: Parameters used in biogeochemical model.

Parameter	Value
δt	6 hours
H	50 m
L	≈670,000 m (6° latitude)
K	130 $m^2\ s^{-1}$
$\bar{C}_{-H}$	2400 μMol kg^{-1}
$C\|^N, C\|_S$	2015 (average value)
$\bar{N}_{-H}$	20.2 μMol kg^{-1}
ΔpCO_2	0.15 C
C (rest)	2015 μMol kg^{-1}

3. Experiments

The model is spun up from rest ($H = 300$ everywhere) for a 20 year period using a monthly wind stress climatology calculated from the FSU monthly mean wind stresses for the period 1961 to 1992 [*Stricherz et al.*, 1992]. The model is then forced by the FSU monthly mean wind stresses for the desired years.

Meridionally averaged output fields of zonal velocity and upwelling (w) as well as meridional velocities along 3°S and 3°N are saved every 6 hours. This interval is chosen to satisfy the Courant-Friedrichs-Lewy (CFL) criterion for numerical stability of the biogeochemical model

$$\frac{c\Delta t}{\Delta x} \leq 1, \tag{8}$$

where c is the propagation speed of the fastest moving disturbance generated by the model; Δt is the model timestep; and Δx is the grid spacing between like variables [*Courant et al.*, 1967]. Since there are no waves in the biogeochemical model, the fastest moving disturbance is the estimated fastest zonal velocity from the hydrodynamic model.

Rearranging equation 8 and estimating $c = 1.0\text{m s}^{-1}$ gives

$$\Delta t \leq \frac{0.25° * (2\pi a/360)}{1.0} \approx 7.7 \text{ hours}, \tag{9}$$

where a is again the equatorial radius of the earth. For simplicity, Δt is chosen to be 6 hours.

The upwelling velocity (w) is calculated from the hydrodynamic model using

$$w = \frac{\Delta h}{\Delta t}. \tag{10}$$

Lastly, the model fields of u, v, and w are averaged over Δt.

The biogeochemical model is run using the equatorial ocean model output for the years 1961 to 1994, plus the observed FSU wind stresses [*Stricherz et al.*, 1992] and the Reynolds SSTs [*Smith et al.*, 1996]. This run, with the full time series inputs of model output fields, SST, and winds, will be referred to as the "basic" model run.

Several different experiments are run to investigate the mechanisms behind the variability in the CO_2 flux (table 3). In particular, 6-hour climatologies are produced from the hydrodynamical model outputs, Reynolds SSTs, and FSU wind stresses (SSTs and wind stresses by linear interpolation from monthly data). The model is then run with various combinations of time series and climatology forcing fields. In addition, an equatorial box model experiment is run where the model is forced by the zonally averaged fields of hydrodynamical model output, Reynolds SSTs, and FSU wind stresses.

Table 3: Model experiments performed. MOF is hydrodynamical model output fields, RSST is the Reynolds sea surface temperatures, and FSUW is the FSU wind stresses.

Run Number	Run Details
1 ("Basic")	MOF, RSST, FSUW time series
2	Box Model (Zonally averaged fields of MOF, RSST, FSUW)
3	MOF, FSUW time series; RSST climatology
4	MOF, RSST time series; FSUW climatology
5	RSST, FSUW time series; MOF climatology

4. Results

Prior to this study, modeling of the ocean-to-atmosphere flux of CO_2 in the equatorial Pacific Ocean was limited to box models [e.g., *Hudson et al.*, 1994; *Craig and Holmen*, 1995; *Murphy*, 1995], and coarse resolution finite difference models [e.g., *Toggweiler et al.*, a1989a; *Sarmiento et al.*, 1992; *Maier-Reimer*, 1993; *Winguth et al.*, 1994]. The results of this research provide an unprecedented opportunity to investigate the physics behind the interannual variability of CO_2 flux from the dominant oceanic source region.

Output fields of C_T, pCO_2, and Q_{CO_2} are saved every ten days for the period 1965-1994. During the first three years of integration (1962-1964) the model equilibrates to the physical forcing and forgets the "memory" due to the initial state.

4.1 Climatology

Ten day anomaly climatologies are constructed from the thirty year time series of C_T, pCO_2, and Q_{CO_2}, in addition to the anomaly climatologies of the input forcing fields of τ, T, u, v, and w (figure 7).

The anomaly climatology of C_T (figure 7a) shows high values of C_T in the easternmost 10° of the basin caused by: (a) strong near-coastal upwelling bringing high concentrations of C_T into the surface layer; and (b) a small but steady eastward zonal current which prevents these high values from being advected away. The low values of C_T in the western warm pool are the result of the minimal upwelling in that region. The large central Pacific region is dominated by a double low, centered in March at 137°W and in October at 129°W. This

double low follows the north/south migration of the intertropical convergence zone (ITCZ) [*Waliser and Gautier*, 1993]. Upwelling is smaller during December through May, resulting in the more pronounced C_T minimum in the first half of the year.

The anomaly climatology of pCO_2 (figure 7b) displays a strong similarity to the anomaly climatology of C_T. The patterns of high values of pCO_2 in the east and the low values of pCO_2 in the west are nearly identical to those of C_T. The double lows of C_T in the central Pacific are mirrored in pCO_2. The minimum value of both C_T and pCO_2 in the second half of the year is more pronounced because the SSTs in July through December are colder than those in January to June.

The results of the anomaly climatology of Q_{CO_2} (figure 7c) indicate that the pattern of CO_2 flux is strongly influenced by equatorial winds. The high values of C_T and pCO_2 in the east are not reflected in Q_{CO_2} because wind speed in the eastern Pacific is low from February to April when the ITCZ is closest to the equator in this region. The low values of C_T and pCO_2 in the western Pacific are enhanced in Q_{CO_2}. This is created by the low wind speeds in this region (especially compared to the rest of the Pacific basin). In the central Pacific the double low in C_T and pCO_2 becomes a double high in Q_{CO_2}, and is shifted in both space and time (to August at 144°W and December at 157°W). These maximums of CO_2 flux closely follow the maximums in wind speed in the central Pacific, indicating a strong influence of wind speed on CO_2 flux.

4.2 Results of basic model run

The thirty year time series of C_T, pCO_2, and Q_{CO_2} are highly variable in space and time, as are the input forcing fields of τ, T, u, v, and w. These fields are examined both as a time averaged zonal anomaly profile with ± 1 standard deviation about the mean, and as a zonally averaged mean anomaly time series with ± 1 standard deviation about the mean anomaly. For reference, the zonal anomaly profiles of the input forcing fields are shown in figure 8 and the anomaly time series of the input forcing fields are shown in figure 9. All the time series profiles have had a one year running average applied to suppress signals on an annual or shorter period. The time series of C_T, pCO_2, and C_T (as well as those of the input forcing fields) are compared against the onset and duration of ENSO warm and cold events as defined by the JMA index [*Japan Meteorological Agency*, 1991]. The red and blue color bars on the time series plots indicate periods of ENSO warm and cold events, respectively.

The zonal anomaly profile of C_T averaged over the entire output time series (figure 10a) in the west is low, but has higher variability than in the rest of the basin. Upwelling is much smaller in this region (figure 8e), leading to lower concentrations of C_T. However, when there is upwelling, the high C_T concentration of the upwelled water causes a large change in the surface water C_T concentration. The C_T concentration in the far east of the basin is high but not as variable. Strong upwelling in this region maintains this high concentration. Over most of the basin, C_T concentration is fairly constant as is the magnitude of the local variability. The values of C_T in the west-central Pacific are slightly higher than those in the east-central Pacific as a result of a mean westward

zonal current in the central portion of the basin (figure 8c).

There is a strong correlation between ENSO and the zonally averaged anomaly time series of C_T (figure 10b). That is, the onset of an ENSO warm event corresponds to a decrease in C_T concentration, while the onset of an ENSO cold event corresponds to an increase in C_T concentration. This trend is seen not only in the zonal mean anomaly C_T time series, but also in the standard deviation about the zonal mean anomaly, suggesting that this is a large-scale effect. This pattern is caused by the change in upwelling due to ENSO. The cessation of equatorial upwelling during an ENSO warm event (as seen in figure 9e) cuts off the major source of new C_T to the surface layer causing to the drop in C_T concentration. In contrast, during an ENSO cold event, upwelling increases, leading to a large influx of new C_T to the surface layer.

The time averaged zonal anomaly profile of pCO_2 (figure 11a) is similar to that of C_T. However, values of pCO_2 in the west are similar to values of pCO_2 in the rest of the basin, while C_T in the west is smaller than C_T in the rest of the basin. This is the result of higher SSTs in this area (figure 8b). The higher SSTs in the western half as compared to those in the eastern half also account for the greater pCO_2 in the western half than in the eastern half when compared to the zonal anomaly profile of C_T.

The zonally averaged anomaly time series of pCO_2 (figure 11b) does not follow the ENSO cycle as closely as C_T. Generally, pCO_2 decreases during a warm event and increases during a cold event. However, the pattern for pCO_2 is not as clear as C_T because of the changes in SST associated with ENSO (figure 9b). Higher SSTs during an ENSO warm event result in higher pCO_2

values, while lower SSTs during an ENSO cold event result in lower pCO_2 values.

The time averaged zonal anomaly profile of Q_{CO_2} (figure 12a) is significantly different from the profiles of both C_T and pCO_2. This is because low wind speeds and their low variability in the west (figure 8a) cause low Q_{CO_2} with little variability. In the far east of the basin there is high CO_2 flux with high variability, a region of high pCO_2, moderate winds, and moderate wind speed variability. While the values of pCO_2 in the far east are high compared to the values in the rest of the basin, this is not significant since the region affected is small compared to the size of the basin. The region of largest CO_2 flux and CO_2 flux variability is in the central Pacific (from about 170°E to 110°W), not in the eastern Pacific where the SST change is the largest. This is because the central Pacific is a region of both large wind speeds and moderately high SSTs.

The zonally averaged anomaly time series of Q_{CO_2} (figure 12b) follows the ENSO cycle more closely than pCO_2 but less than closely than C_T. For most of the ENSO events, Q_{CO_2} decreases during an ENSO warm event and increases during an ENSO cold event. The reason for this is that the equatorial trade winds are, in general, weaker during an ENSO warm event and stronger during an ENSO cold event (figure 9a). However, during longer duration events (e.g., warm events in 1969, 1982-83, 1986, and 1991; cold events in 1970, 1974), Q_{CO_2} decreases at the beginning of a warm event and then increases, while at the beginning of a cold event Q_{CO_2} increases and then decreases. This is because the trade winds (figure 9a) and upwelling (figure 9e) begin returning to normal prior to the end of the event.

4.3 Model comparisons

Several different experiments are run to determine the physical mechanisms behind the interannual variability of Q_{CO_2} from the equatorial Pacific (table 3). The box model experiment (# 2) and the climatological physics experiment (# 5) are run to determine the importance of the upper layer physics in interannual Q_{CO_2} variability. The climatological SST experiment (# 3) is run to show the importance of SST as a primary effect, and the climatological winds experiment (# 4) is run to examine the contribution of the winds to interannual variability.

The box model experiment is run with the zonally averaged (124°E - 77°W) forcing fields of hydrodynamic model output, Reynolds SSTs, and Florida State winds. The zonally averaged anomaly time series of C_T (figure 13a) from both experiments roughly follow each other with the largest differences starting in 1985. The plot of relative difference (figure 13b) indicates that C_T in the basic model run decreases much more during an ENSO warm event and increases much more during an ENSO cold event.

The zonally averaged anomaly time series of pCO_2 obtained from the box model and the basic model run (figure 14a) are similar to those of C_T (figure 13a). The plot of relative difference (figure 14b) highlights the main distinction between C_T and pCO_2. That is, that the relative difference in pCO_2 between the box model and the basic model run is 10 times larger than the relative difference in C_T between the two models. Further, while the mean relative difference in C_T is -0.1 (box model C_T slightly larger than in the basic model run), the mean relative difference in pCO_2 is 1.7 (basic model run pCO_2 higher than box model).

The Q_{CO_2} produced using the two models (figure 15) is not as closely correlated as either the C_T or pCO_2 was using the two models. This is because the box model misses some cold events entirely (e.g., 1970 and 1988). As a result, the plot of relative difference (figure 15b) shows that basic model run Q_{CO_2} is nearly always higher than box model Q_{CO_2}.

Results from the box model run reveal the importance of a zonal structure in explaining the physics of ocean-to-atmosphere CO_2 flux, but do not explain the relative contribution of the input forcing fields to the interannual variability. The physics involved in the variability is more closely explored by running separate model experiments with climatological forcing fields for hydrodynamic model output, SST, and winds.

Next, the results of the basic model run are compared with the results of the model forced by climatological SSTs. During these experiments, the model is also forced by the hydrodynamic model output and the winds from same the 33 year time series (1962-1994) used in the basic model run.

When forced by climatological SSTs the model shows little difference in C_T (figure 16). There is a maximum relative difference of about 0.05% and a pattern that demonstrates that C_T in the climatological SST run is smaller than in the basic model run during an ENSO warm event, but larger than in the basic model run during an ENSO cold event.

While the pCO_2 differs more between the climatological SST run and the basic model run (figure 17) than does the C_T, the difference is still small. Since pCO_2 is determined as a function of C_T and SST (Appendix B), the warmer SSTs during an ENSO warm event lead to larger pCO_2 in the basic model run,

while the colder SSTs during an ENSO cold event result in smaller pCO_2 in the basic model run. Outside of an ENSO event the difference between the two runs is negligible. Thus, the plots of zonally averaged anomaly time series (figure 17a) nearly overlay each other in the periods between ENSO events.

The difference in Q_{CO_2} produced during the two runs (figure 18) is virtually identical to the difference in pCO_2 (figure 17). This indicates the temperature effects of ocean-to-atmosphere CO_2 flux are small when the temperature range is small, as has been shown to be the case in the equatorial Pacific [*Wanninkhof*, 1992].

The results of the model experiment forced by climatological winds are more dramatic, especially for Q_{CO_2}, than the results for the climatological SST run. As in the climatological SST run, the greatest deviations between the climatological winds run and the basic model run occur during ENSO events (figure 19a). However, the relative difference between the climatological winds run and the basic model run (figure 19b) are of opposite sign and about four times larger than the relative difference resulting from the climatological SST run (higher C_T in basic model run during ENSO warm event, lower C_T during ENSO cold event). In addition, in contrast to the climatological SST run the zonally averaged anomaly time series of the climatological winds run and the basic model run also differ during non-ENSO periods.

The differences between the two runs appear small at first glance, particularly in the zonally averaged relative difference (figure 20). However, the two runs have contrasting zonal profiles (not shown) which offset their relative difference. In comparison to pCO_2 in the climatological winds run, the pCO_2 in

the basic model run is larger in the central Pacific and smaller in the eastern and western Pacific.

The largest deviations between the climatological wind run and the basic model run occur in Q_{CO_2} (figure 21). The climatological winds run misses much of the variability associated with ENSO, notably during 1970, 1975, 1988, and 1991 as illustrated in the plot of the zonally averaged anomaly time series (figure 21a). Most of these are ENSO cold events. The plot of relative difference (figure 21b) confirms that the largest differences occur during a cold event, where Q_{CO_2} from the basic model run exceeds that of the climatological winds run.

The last model experiment run used the climatology of the hydrodynamic model output ("climatological physics run"). The results of this experiment exhibited the largest deviations from the basic model run. This is because C_T in the climatological physics run reproduces none of the interannual variability associated with ENSO (figure 22a). When compared to the basic model run, the climatological physics run has about 25% of the variability in C_T. The plot of the zonally averaged relative difference (figure 22b) shows that the climatological physics run always underestimates the C_T produced from the basic model run, with an average offset of 1.3%.

The link between carbon chemistry and ENSO can be seen in the results of pCO_2 produced from the climatological physics run (figure 23a). While the comparison of C_T between the climatological physics run and the basic model run (figure 19) shows that C_T in the climatological physics run has none of the interannual variability found in the basic model run, the pCO_2 produced from the climatological physics run does reflect the interannual variability associated

with ENSO. This is due to SST (figure 9b), since pCO_2 is a function of SST and C_T only, and C_T (figure 19) demonstrates no connection with the ENSO cycle. The connection of pCO_2 to ENSO warm events is strong, but becomes attenuated during an ENSO cold event. This is further demonstrated in the plot of zonally averaged relative difference (figure 23b), where the relative difference between pCO_2 produced from the climatological physics run and pCO_2 produced from the basic model run increases during an ENSO cold event and decreases during an ENSO warm event. The mean offset between the climatological physics run and the basic model run is significantly larger with respect to pCO_2 (with a mean value of over 15%), than the mean offset with respect to C_T (as seen in figure 22b).

The zonally averaged anomaly time series of Q_{CO_2} for the climatological physics run reproduces more of the interannual variability (figure 24), although significant deviations still exist in some years (e.g., 1978, 1975, 1983, 1987). The zonally averaged relative difference between the climatological physics run and the basic model run (figure 24b) still demonstrates a large mean offset of more than 15%, and has the same pattern as the plot of zonally averaged relative difference of pCO_2 (figure 23b), indicating the relative difference decreases during an ENSO warm event and increases during an ENSO cold event.

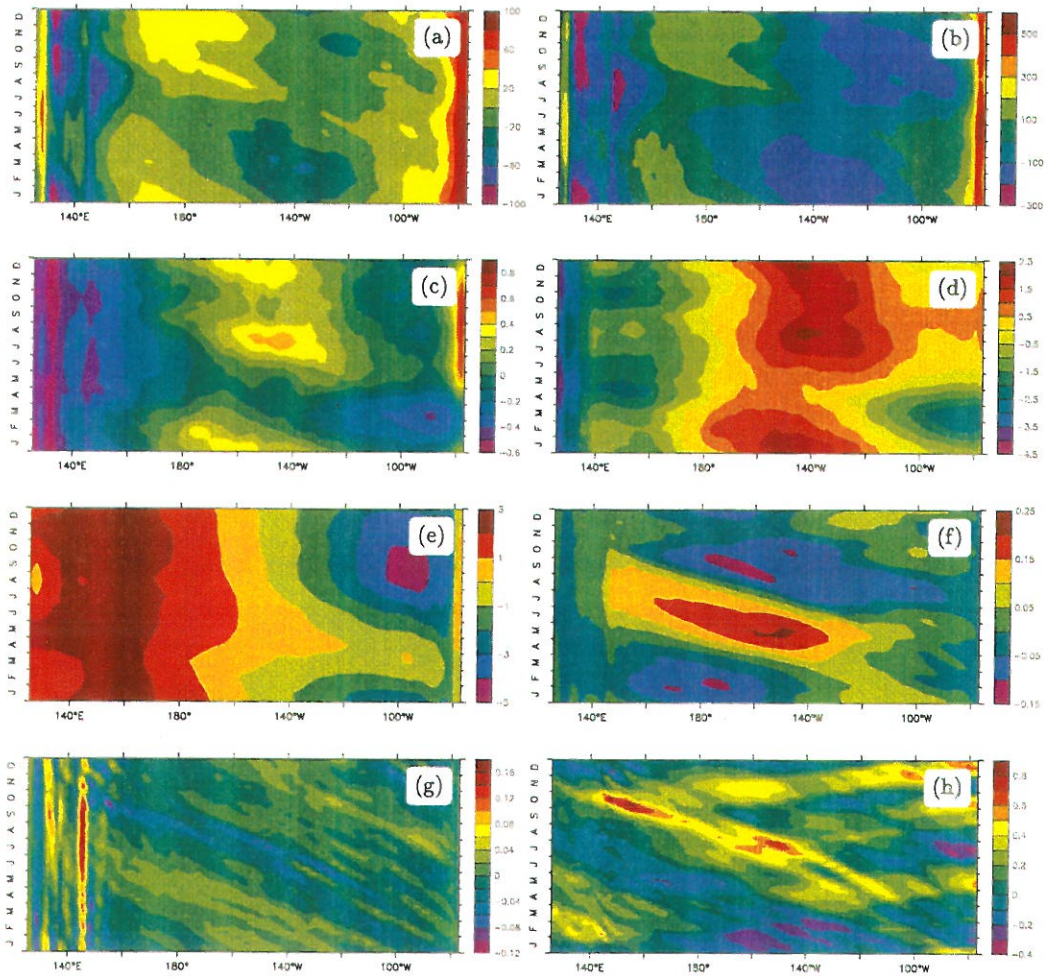


Figure 7: Hovmüller diagrams of Ten-day Anomaly Climatologies. (a) Anomaly climatology of C_T (μMol kg^{-1}). The double low pattern seen in the central Pacific is caused by both upwelling (which is weaker from December to May, figure 7h) and wind speed (which is weaker from March to June, figure 7d). High values of C_T in the easternmost region are caused by both upwelling and a small but steady eastward ocean current. (b) Anomaly climatology of pCO_2 (μatm). The pattern in pCO_2 is similar to that of C_T. The difference in the later part of the year is caused by the cold SST, east of 140°W, from July through January (figure 7e). (c) Anomaly climatology of Q_{CO_2} (10^{-3} Gt$-$C yr^{-1}). The pattern of Q_{CO_2} is strongly influenced by the strength of the equatorial trades. The equatorial trades are weak in the eastern Pacific from December through May, and weak in the central Pacific from March to June. (d) Anomaly climatology of τ (m^2 s^{-2}). (e) Anomaly climatology of SST (°C). (f) Anomaly climatology of u (m s^{-1}). (g) Anomaly climatology of v (m s^{-1}). (h) Anomaly climatology of w (m day^{-1}).

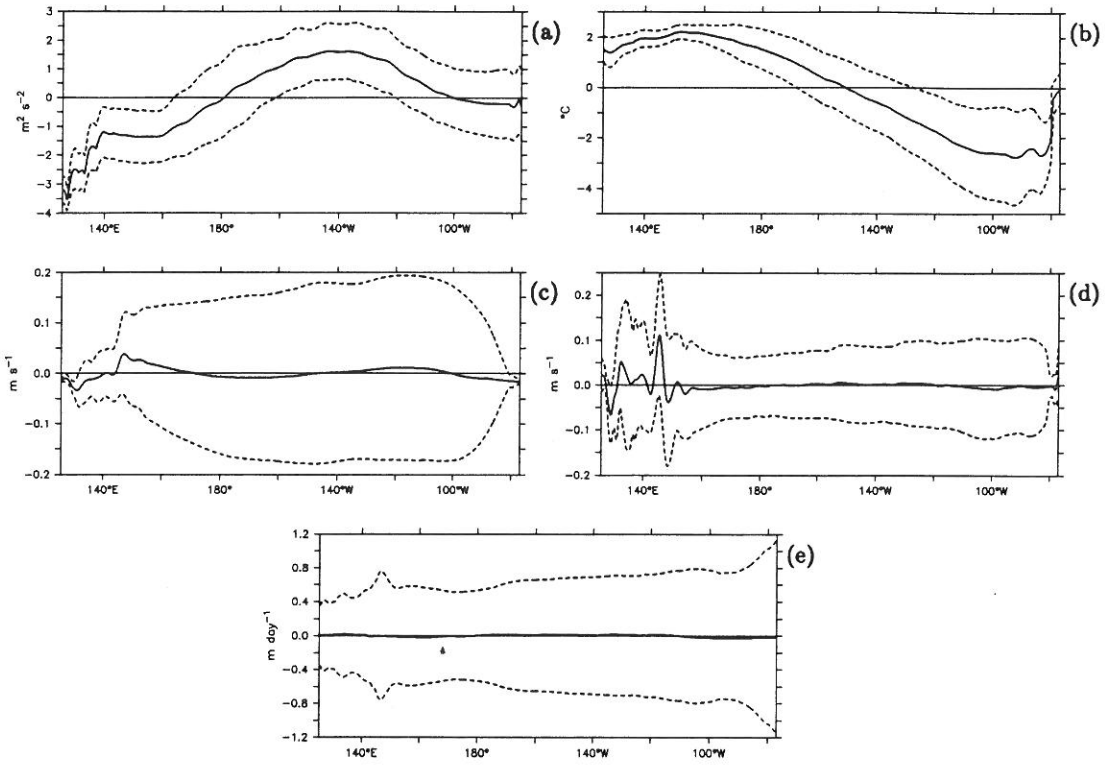


Figure 8: Time averaged zonal anomaly profiles of input forcing fields. The black line is the mean profile, the dashed lines are ± 1 standard deviation about this mean. (a) Zonal anomaly profile of τ ($m^2\,s^{-2}$). (b) Zonal anomaly profile of SST (°C). (c) Zonal anomaly profile of u ($m\,s^{-1}$). (d) Zonal anomaly profile of v ($m\,s^{-1}$). (e) Zonal anomaly profile of w ($m\,day^{-1}$) (the mean anomaly of w has been enhanced by a factor of 10 to show detail).

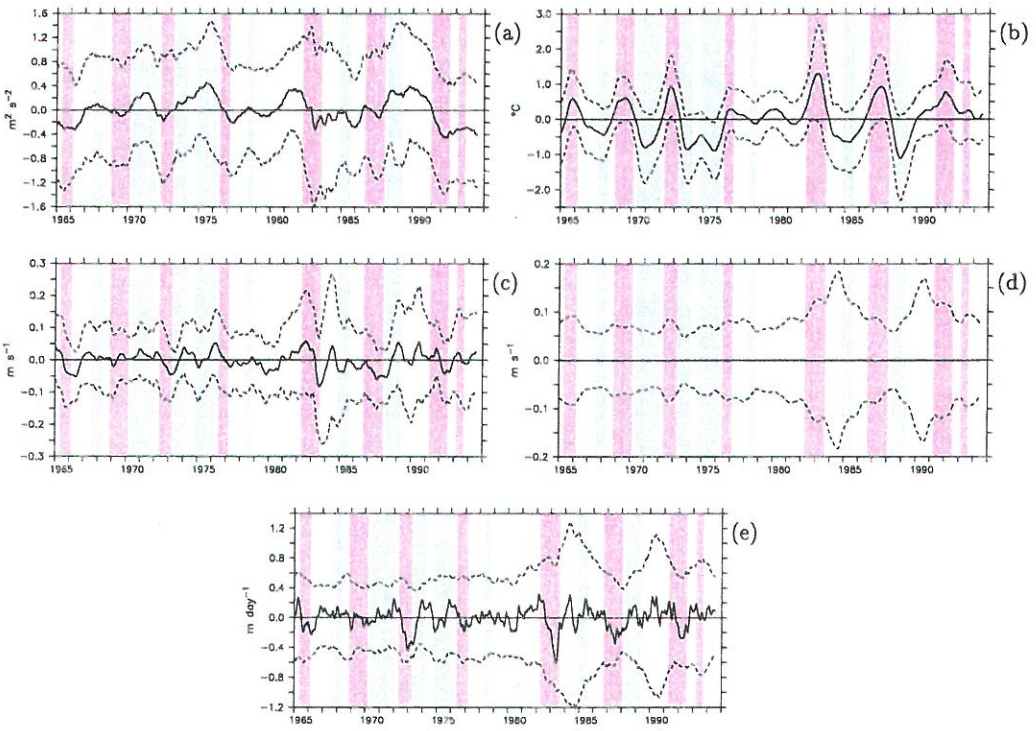


Figure 9: Zonally averaged anomaly time series of input forcing fields. The black line represents the mean profile of C_T, the dashed lines are ± 1 standard deviation about this mean. The red bars show periods of ENSO warm events, and the blue bars show periods of ENSO cold events (as given by the JMA index). (a) Zonal anomaly profile of τ ($m^2\,s^{-2}$). (b) Zonal anomaly profile of SST (°C). (c) Zonal anomaly profile of u ($m\,s^{-1}$). (d) Zonal anomaly profile of v ($m\,s^{-1}$). (e) Zonal anomaly profile of w ($m\,day^{-1}$) (the mean anomaly of w has been enhanced by a factor of 5 to show detail).

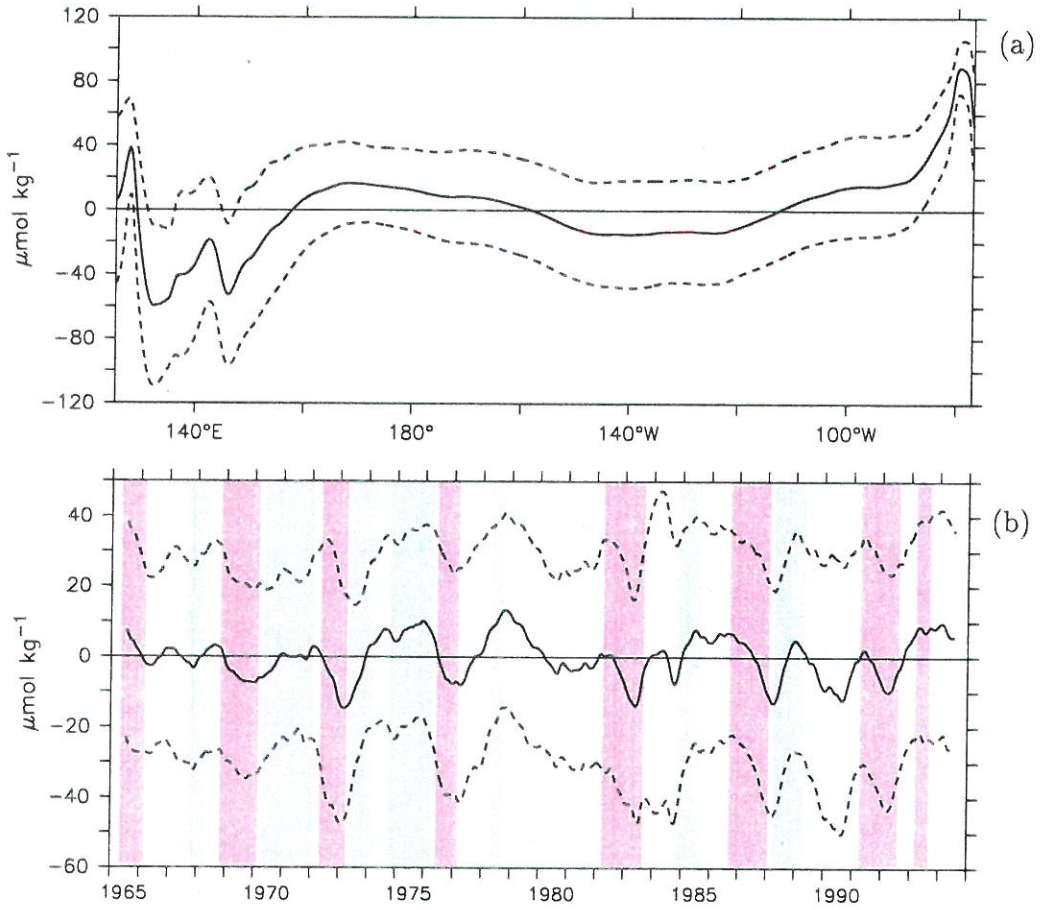


Figure 10: Model results of C_T. The black line is the average anomaly of C_T, the red lines are ± 1 standard deviation about this average. (a) Time averaged zonal anomaly profile of C_T. C_T is lowest in the western warm pool, and highest in the eastern upwelling region. Variability in C_T is mostly constant over the interior of the domain. (b) Zonally averaged anomaly time series of C_T (1 year running average applied). The red bars show periods of ENSO warm events, and the blue bars show periods of ENSO cold events (as given by the JMA index). C_T decreases during warm events and increases during cold events.

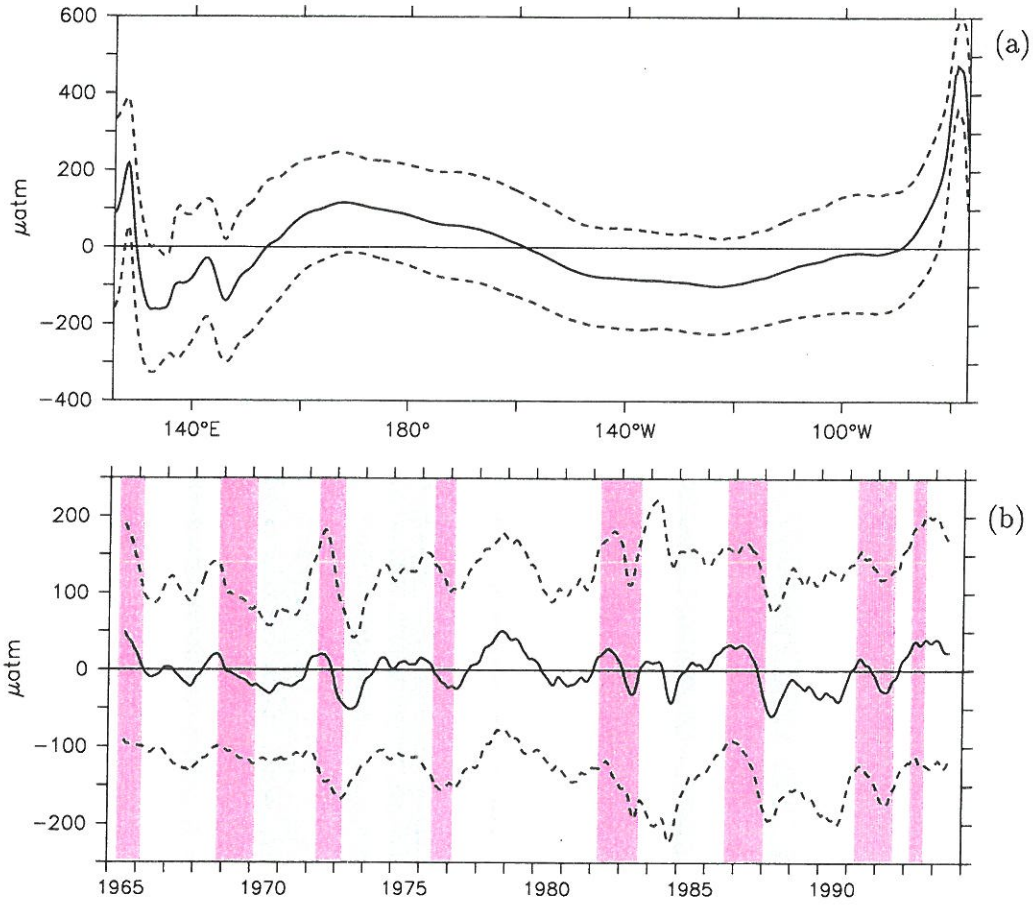


Figure 11: Model results of pCO_2 (lines are as defined for C_T in figure 10). (a) Time averaged zonal anomaly profile of pCO_2. pCO_2 profile is similar to C_T, except the low in the warm pool is smaller in pCO_2 and the mean anomaly profile (black line) deviates more from zero. (b) Zonally averaged anomaly time series of pCO_2 (1 year running average applied). pCO_2 does not follow ENSO warm and cold events as closely as C_T. In general, pCO_2 decreases during warm events and increases during cold events, but counter examples exist (e.g., 1967, 1975, 1993).

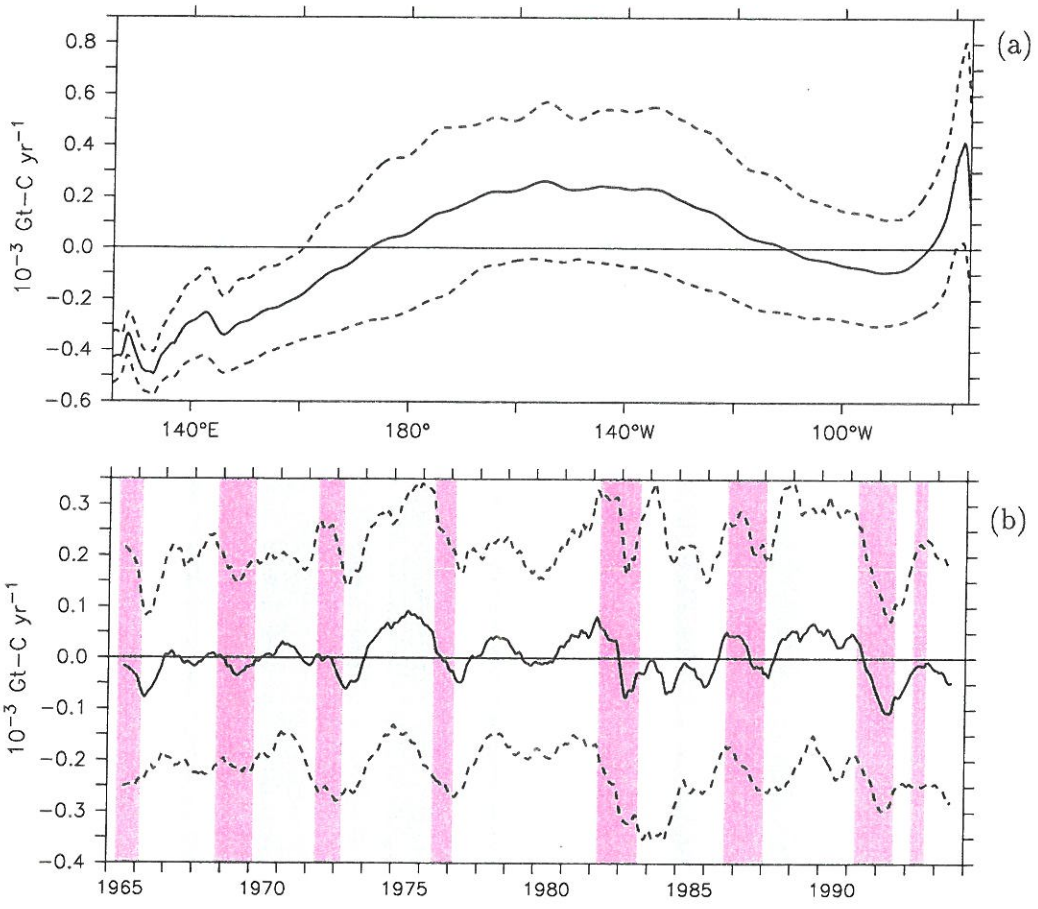


Figure 12: Model results of Q_{CO_2} (per unit area; lines are as defined for C_T in figure 10). (a) Time averaged zonal anomaly profile of Q_{CO_2}. Except for a narrow region in the far east, most of the flux and flux variability is located in the central equatorial Pacific Ocean, from about 170°E to 110°W. (b) Zonally averaged anomaly time series of Q_{CO_2} (1 year running average applied). Q_{CO_2} follows the ENSO cycle more closely than pCO_2 but not as close as C_T. Flux is stronger during ENSO cold events and weaker during ENSO warm events (except for 1967 and 1993).

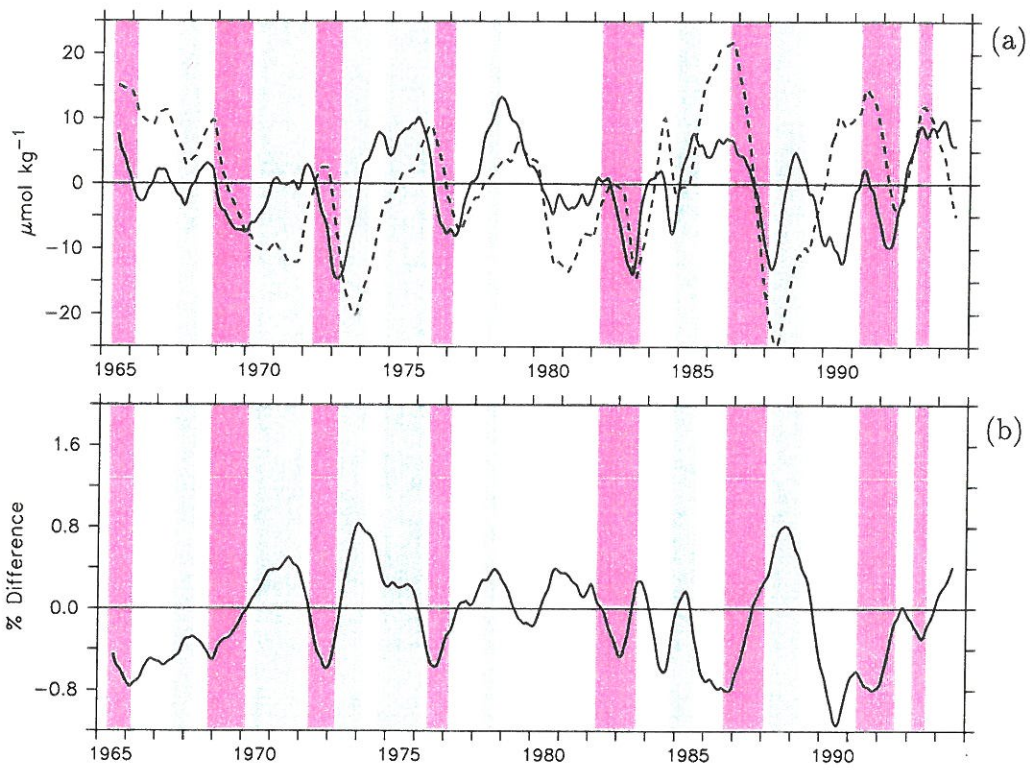


Figure 13: C_T comparison with box model. (a) Zonally averaged anomaly C_T from the biogeochemical model (black line) and the box model (dashed line), with a 1 year running average applied to both curves. (b) Zonally averaged relative difference in C_T between the biogeochemical model and the box model, with a 1 year running average applied. ENSO warm events are shown by red bars, ENSO cold events by blue bars. The curves roughly follow each other until 1985.

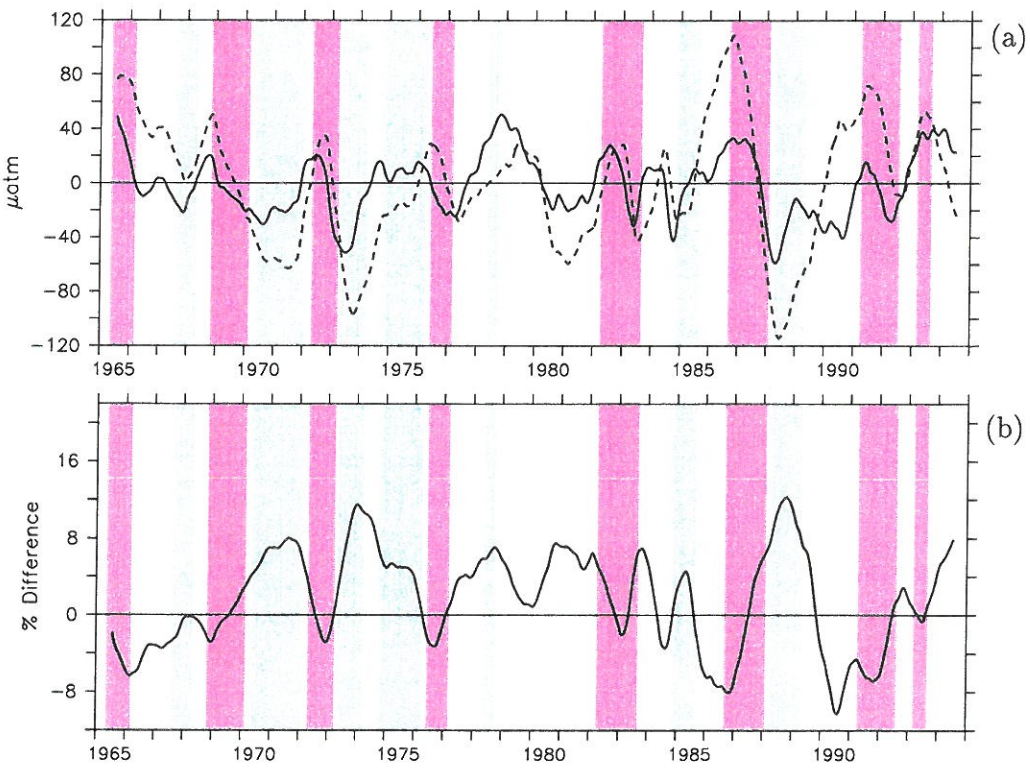


Figure 14: pCO_2 comparison with box model. (a) Zonally averaged anomaly pCO_2 from the biogeochemical model (black line) and the box model (dashed line), with a 1 year running average applied to both curves. (b) Zonally averaged relative difference in pCO_2 between the biogeochemical model and the box model, with a 1 year running average applied. ENSO warm events are shown by red bars, ENSO cold events by blue bars. Differences seen in C_T are exaggerated here, large departures can be seen in 1970-1975, as well as after 1985.

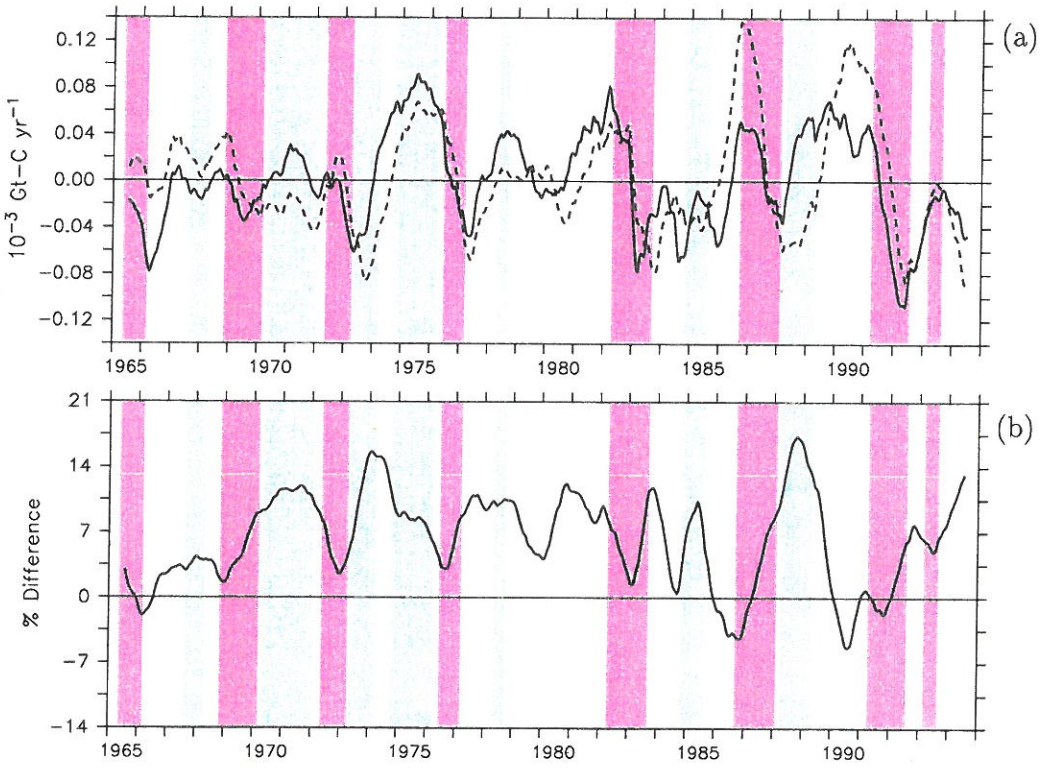


Figure 15: Q_{CO_2} (per unit area) comparison with box model. (a) Zonally averaged anomaly Q_{CO_2} from the biogeochemical model (black line) and the box model (dashed line), with a 1 year running average applied to both curves. (b) Zonally averaged relative difference in Q_{CO_2} between the biogeochemical model and the box model, with a 1 year running average applied. ENSO warm events are shown by red bars, ENSO cold events by blue bars. There is a large offset from 1966 to 1985, with the largest error being in 1988.

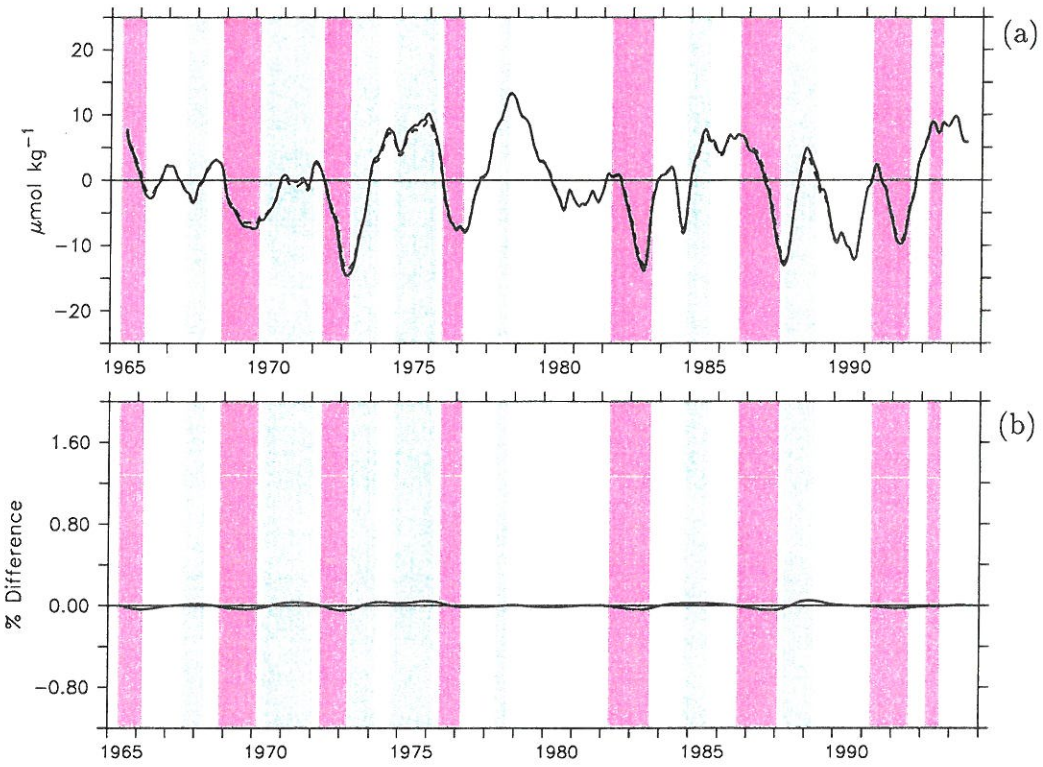


Figure 16: C_T comparison with model forced by climatological SST. (a) Zonally averaged anomaly C_T from the basic model run (black line) and the climatological SST run (dashed line), with a 1 year running average applied to both curves. (b) Zonally averaged relative difference in C_T between the basic model run and the climatological SST run, with a 1 year running average applied. ENSO warm events are shown by red bars, ENSO cold events by blue bars. Differences in C_T between the two model runs are negligible.

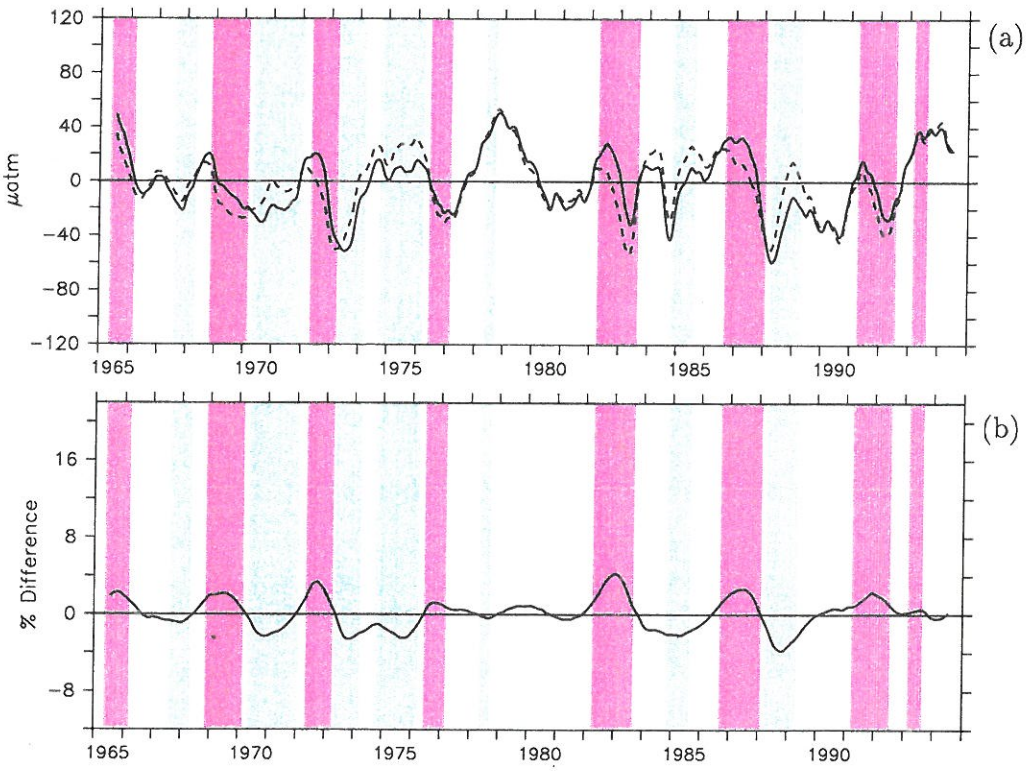


Figure 17: pCO_2 comparison with model forced by climatological SST. (a) Zonally averaged anomaly pCO_2 from the basic model run (black line) and the climatological SST run (dashed line), with a 1 year running average applied to both curves. (b) Zonally averaged relative difference in pCO_2 between the basic model run and the climatological SST run, with a 1 year running average applied. ENSO warm events are shown by red bars, ENSO cold events by blue bars. The two curves follow each other closely with lower pCO_2 in the climatological SST run during a warm event and higher pCO_2 during a cold event.

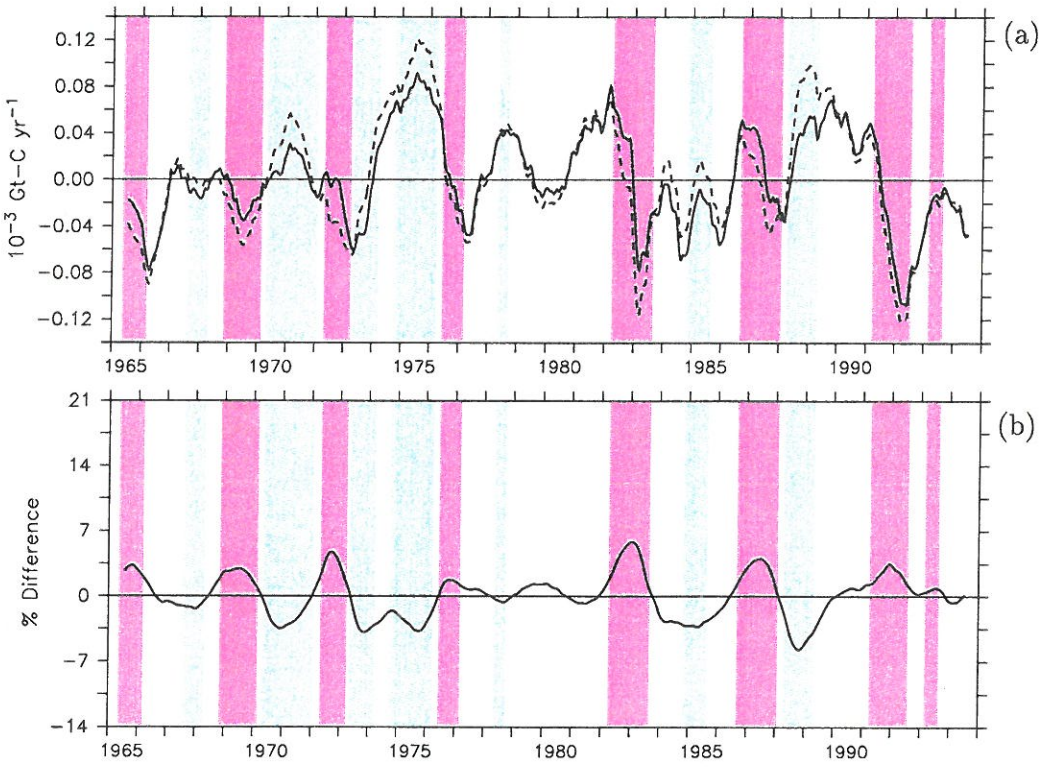


Figure 18: Q_{CO_2} (per unit area) comparison with model forced by climatological SST. (a) Zonally averaged anomaly Q_{CO_2} from the basic model run (black line) and the climatological SST run (dashed line), with a 1 year running average applied to both curves. (b) Zonally averaged relative difference in Q_{CO_2} between the basic model run and the climatological SST run, with a 1 year running average applied. ENSO warm events are shown by red bars, ENSO cold events by blue bars. Same pattern as for pCO_2 (figure 17), but a slightly larger relative difference between the two runs.

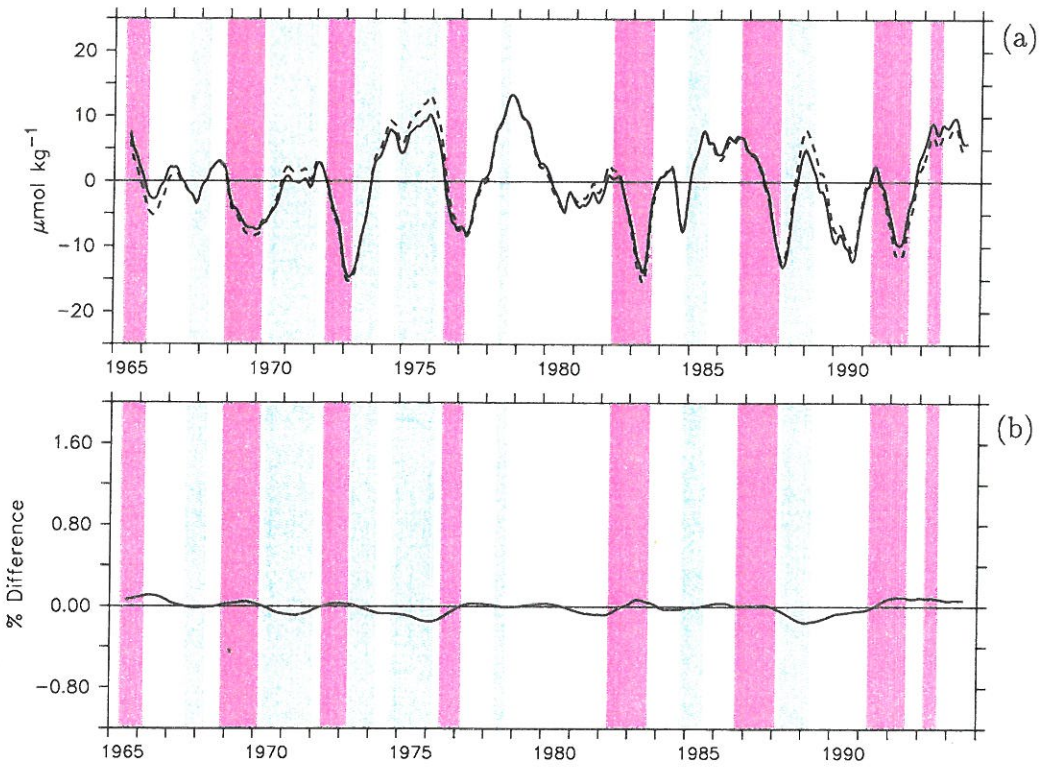


Figure 19: C_T comparison with model forced by climatological winds. (a) Zonally averaged anomaly pCO_2 from the basic model run (black line) and the climatological wind run (dashed line), with a 1 year running average applied to both curves. (b) Zonally averaged relative difference in pCO_2 between the basic model run and the climatological wind run, with a 1 year running average applied. ENSO warm events are shown by red bars, ENSO cold events by blue bars. The difference in C_T between the two runs is larger than in the climatological SST run and reversed with respect to the ENSO cycle (figure 16), with more C_T in the climatological winds run during a warm event and less C_T during a cold event.

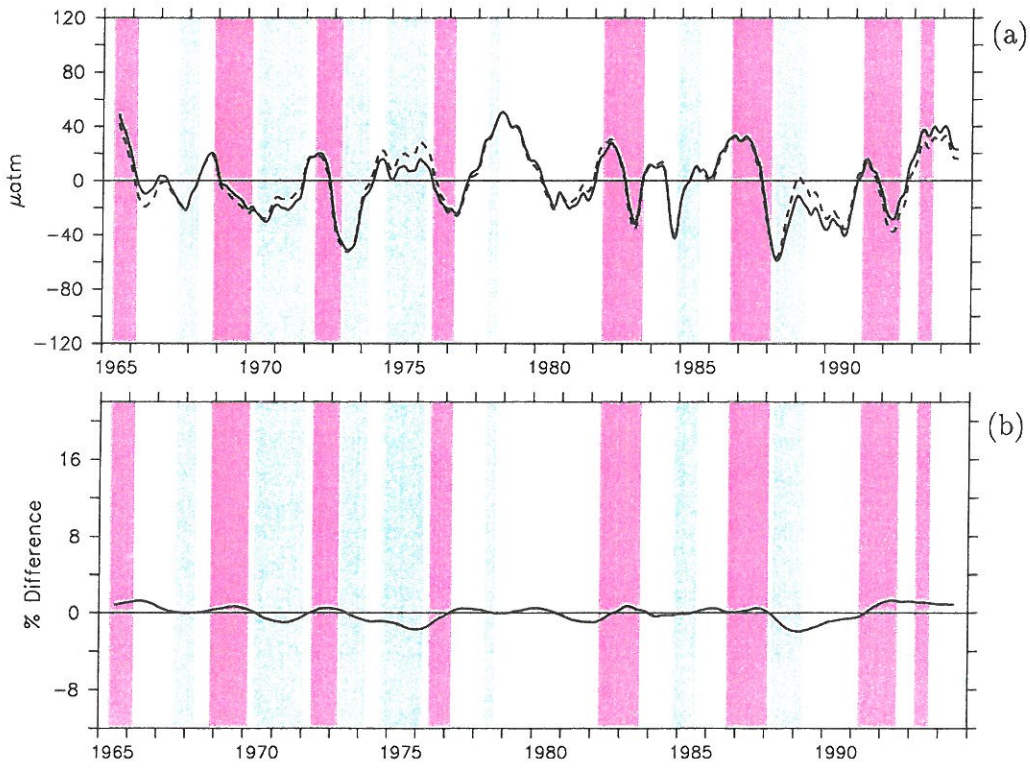


Figure 20: pCO_2 comparison with model forced by climatological winds. (a) Zonally averaged anomaly pCO_2 from the basic model run (black line) and the climatological wind run (dashed line), with a 1 year running average applied to both curves. (b) Zonally averaged relative difference in pCO_2 between the basic model run and the climatological wind run, with a 1 year running average applied. ENSO warm events are shown by red bars, ENSO cold events by blue bars. The results for pCO_2 are similar to C_T (figure 19), but with a larger relative difference between the two runs.

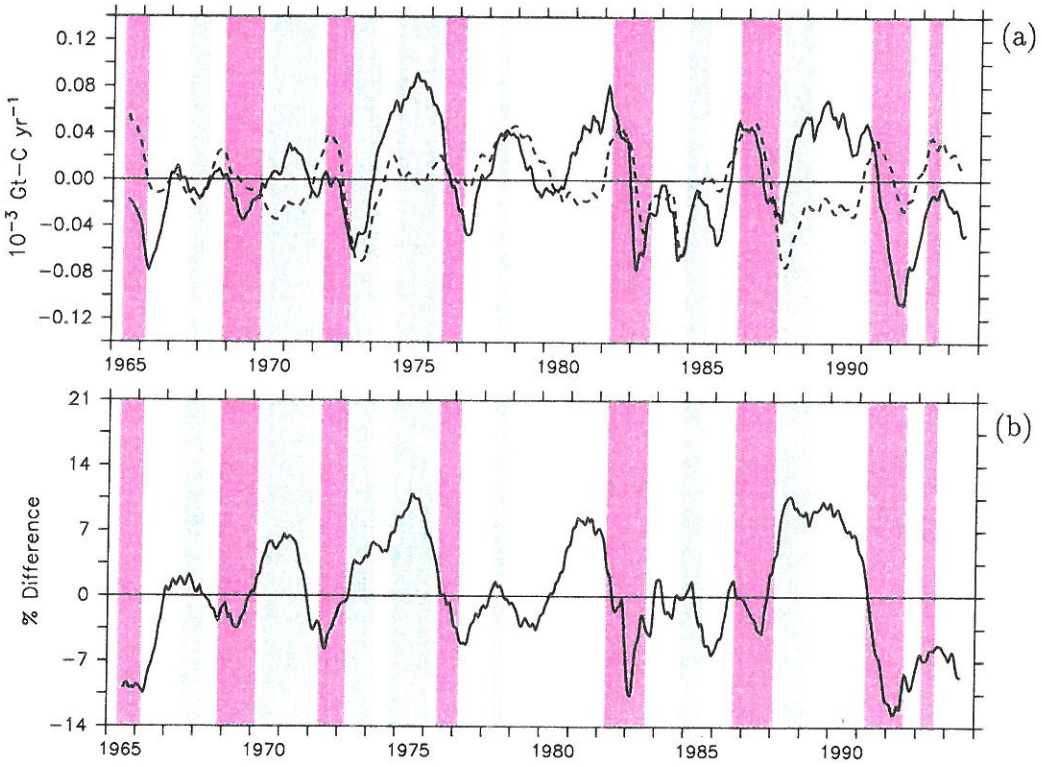


Figure 21: Q_{CO_2} (per unit area) comparison with model forced by climatological winds. (a) Zonally averaged anomaly Q_{CO_2} from the basic model run (black line) and the climatological wind run (dashed line), with a 1 year running average applied to both curves. (b) Zonally averaged relative difference in Q_{CO_2} between the basic model run and the climatological wind run, with a 1 year running average applied. ENSO warm events are shown by red bars, ENSO cold events by blue bars. Large differences between the two curves can be seen here. Q_{CO_2} in the climatological wind run is much larger during a warm event, and much smaller during a cold event.

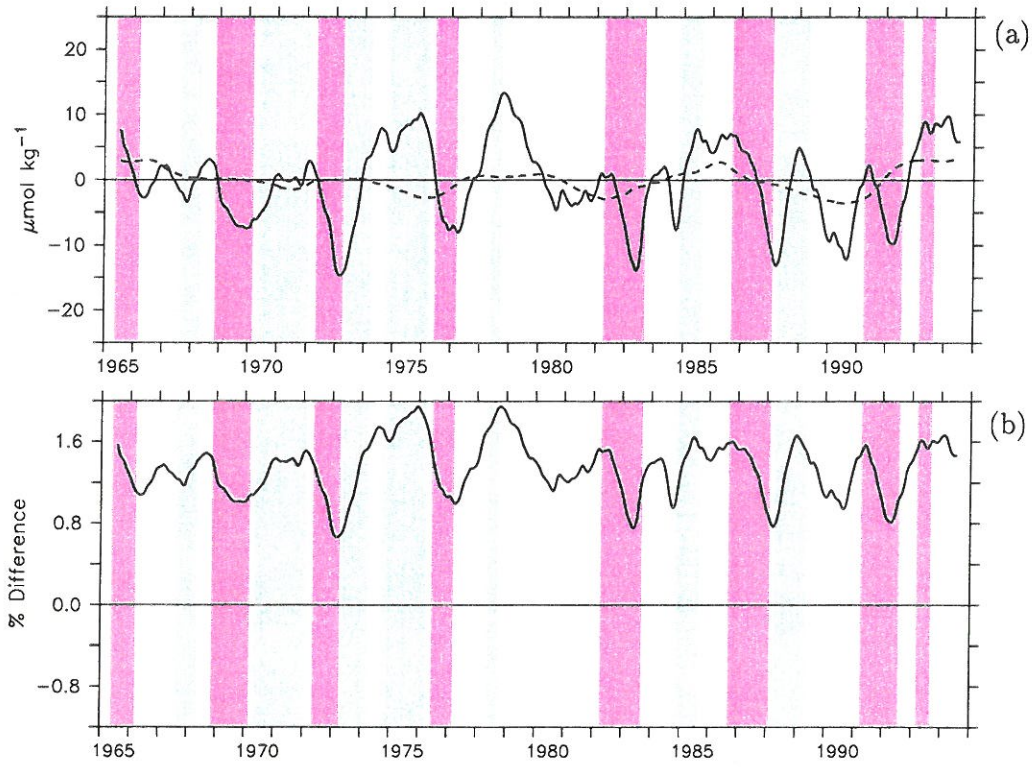


Figure 22: C_T comparison with model forced by climatological physics. (a) Zonally averaged anomaly C_T from the basic model run (black line) and the climatological physics run (dashed line), with a 1 year running average applied to both curves. (b) Zonally averaged relative difference in C_T between the basic model run and the climatological physics run, with a 1 year running average applied. ENSO warm events are shown by red bars, ENSO cold events by blue bars. The climatological physics run misses all the interannual variability seen in the basic model run. While the relative difference between the two runs is not that large, it is still 100 times larger than the relative difference in the climatological SST run (figure 16b), and 10 times larger than the relative difference in the climatological wind run (figure 19b). In addition, the relative difference is always positive with C_T in the climatological physics run always less than in the basic model run.

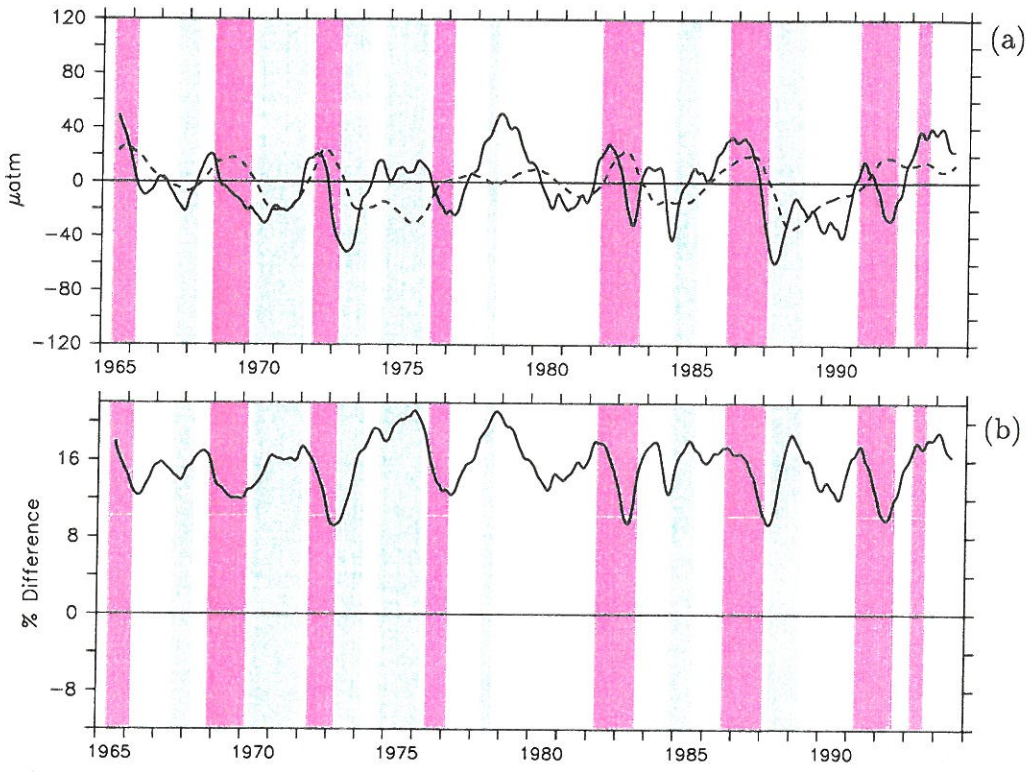


Figure 23: pCO_2 comparison with model forced by climatological physics. (a) Zonally averaged anomaly pCO_2 from the basic model run (black line) and the climatological physics run (dashed line), with a 1 year running average applied to both curves. (b) Zonally averaged relative difference in pCO_2 between the basic model run and the climatological physics run, with a 1 year running average applied. ENSO warm events are shown by red bars, ENSO cold events by blue bars. The 1-2% relative difference in C_T (figure 22b) becomes a 10-20% difference in pCO_2. The climatological physics run captures some of the interannual variability in pCO_2. The relative difference is again always positive, with the pCO_2 in the climatological physics run always less than that in the basic model run.

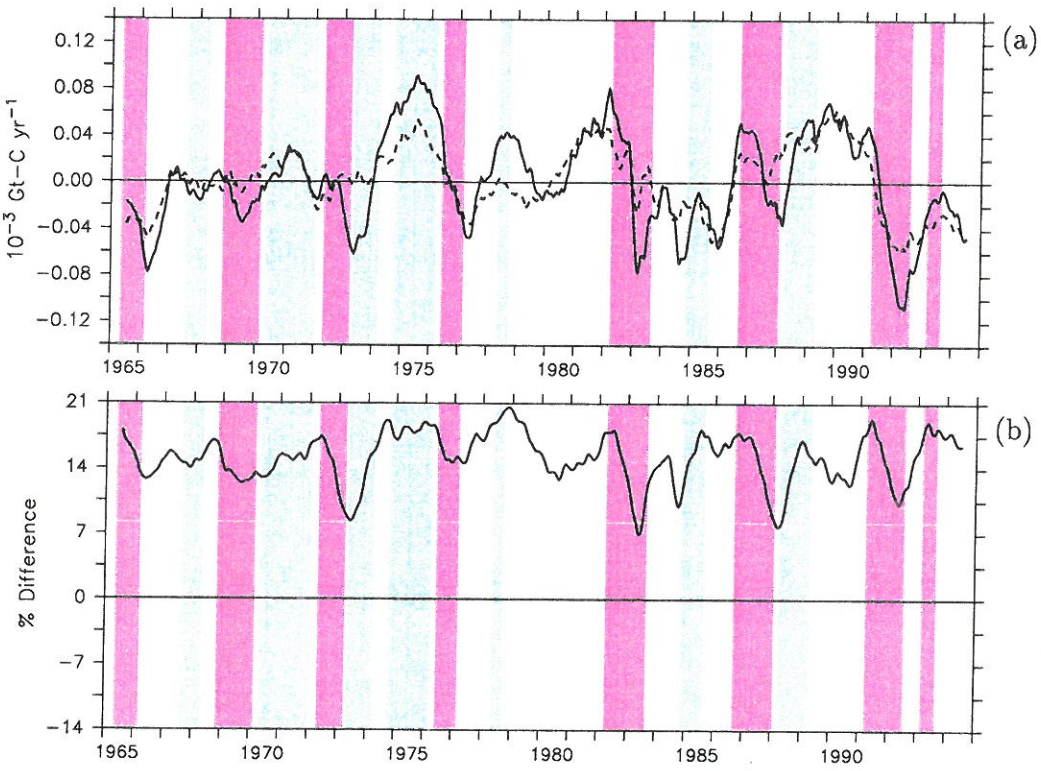


Figure 24: Q_{CO_2} (per unit area) comparison with model forced by climatological physics. (a) Zonally averaged anomaly Q_{CO_2} from the basic model run (black line) and the climatological physics run (dashed line), with a 1 year running average applied to both curves. (b) Zonally averaged relative difference in Q_{CO_2} between the basic model run and the climatological physics run, with a 1 year running average applied. ENSO warm events are shown by red bars, ENSO cold events by blue bars. There is still a large difference as in pCO_2 (figures 23), but a little more of the interannual variability in Q_{CO_2} is reproduced in the climatological physics run. The relative difference is always greater than 0 (as in C_T and pCO_2), indicating that the climatological physics run always underestimates Q_{CO_2}.

5. Comparison With Observational Data

5.1 Ocean carbon measurements

As stated in the introduction, there have been no long term measurements of ocean-to-atmosphere CO_2 flux, or related quantities, in the equatorial Pacific Ocean. There have been many studies measuring C_T, pCO_2, ΔpCO_2, and/or Q_{CO_2} on a limited temporal or spatial range. Due to their limited observation duration these studies are not useful in examining interannual variability. However, some researchers have made measurements for periods of 1 to 3 years. This observational data was compared to the results presented in this study as a means of validating the model.

Wong et al. [1993] estimated Q_{CO_2} between hydrographic and chemistry data collected from 1985 to 1988, during which time there was one ENSO cold event (1985) and one ENSO warm event (1986). They estimated Q_{CO_2} values over the region between 170°W to 180° for two latitudinal ranges, 5°S-0° and 0°-5°N. If the estimated Q_{CO_2} values from Wong are summed and compared against the basic model run Q_{CO_2} from this study (averaged from 170°W-180° over the same time period), a similar pattern can be seen (figure 25).

The CO_2 flux values from the basic model run and the Wong data demonstrate good correlation with the exception of the first part of 1985. Both curves have a peak in mid 1986, drop to low levels in 1987, and rise again in early 1988. The ENSO cold event during the first half of 1985 explains the high values in the model, but does not account for the low values in the observational data. The ENSO warm event that starts in the last months of 1986 and continues through 1987 produces the low CO_2 flux values found in both the model and in

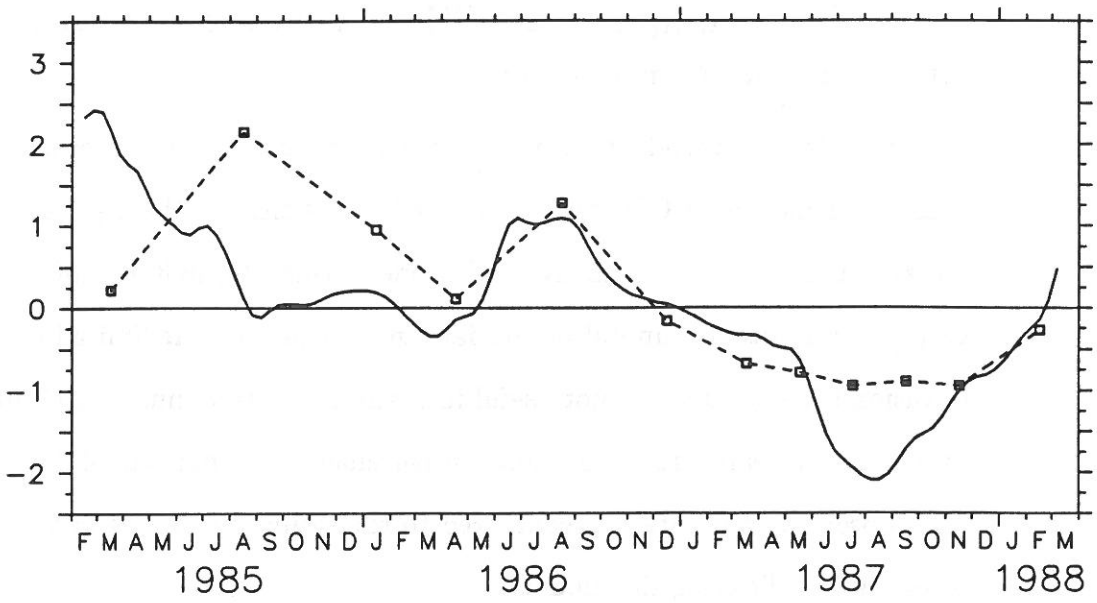


Figure 25: Comparison between model Q_{CO_2} (solid line) and Q_{CO_2} estimate from *Wong et al.* [1993] (squares with dashed line the linear interpolation between values). Values from both sources have been normalized for comparison. The model values are averaged over 170°W to 180°.

Wong's data. In addition, both CO_2 flux estimates exhibit the recovery from the warm phase in early 1988.

Dandonneau [1995] took measurements of pCO_2 from August 1991 to October 1992 in the eastern equatorial Pacific. During most of the observation period there was an ENSO warm event which ended in July, 1992. A comparison of pCO_2 produced from the basic model run of this study and the observational data from Dandonneau also demonstrates good agreement over the entire time period (figure 26). Both the pCO_2 from the model and the observational data drop during the period of the ENSO warm event and begin to recover after the event ends.

Inoue et al. [1996] examined the longitudinal distribution of pCO_2 for two

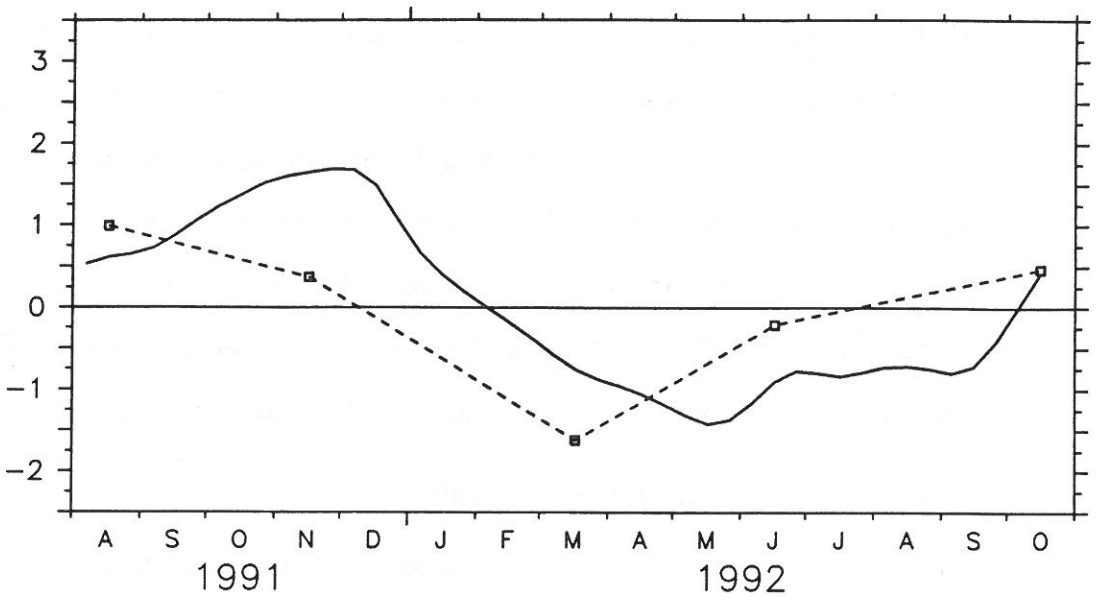


Figure 26: Comparison between model pCO_2 (solid line) and pCO_2 estimate from *Dandonneau* [1995] (squares with dashed line the linear interpolation between values). Values from both sources have been normalized for comparison.

different periods, January-February 1994 and November-December 1994. During January-February 1994 pCO_2 was constant in the western Pacific (140°E-170°E), gradually decreasing to the east. At 170°E pCO_2 rises steeply, leveling off at 170°W some 100 μatm higher than in the western Pacific. The profile produced by the model during this period is similar: flat in the west, rising sharply in the central Pacific before leveling out, except that the sharp increase happens at 160°E. In contrast to the pCO_2 profile during the January-February 1994 period, the longitudinal distribution from both the data and the basic model run differ markedly during the November-December 1994 period. The profile from the observational data is flat from 150°E to 165°W, rising only slightly to the east. The model profile is also flat during the November-December 1994 pe-

riod, although not as flat as the observational data. The differences between the observational data and the model results can partially be attributed to the differences in the spatial and temporal distribution of the two data sets. While the observational profiles are from a series of measurements along the equator starting at the beginning of the specific period in the western Pacific and ending in the central Pacific at the end of the period, the model profile is constructed from the average over the time period at each point along the equator.

5.2 Oceanic proxy measurements

Since there is a dearth of observational oceanic carbon data to compare to the model results, the model will validated using other variables with a longer, more continuous time series. Because many researchers have noted a connection between CO_2 flux and ENSO [e.g., *Feely et al.*, 1987], a comparison between an ENSO index and the model CO_2 flux is appropriate.

The JMA index is one of the methods used to define the onset and duration of ENSO warm and cold events [*Japan Meteorological Agency*, 1991]. In the results section of this study, the model was visually compared to these events as defined by the JMA index. A cross correlation (not shown) between the JMA index from 1965 to 1994 with the model CO_2 flux shows a maximum correlation coefficient of R=-0.53 with a 6 month lag. This means that high values of the JMA index precede the minimum CO_2 flux from the ocean model by 6 months, and low values lead CO_2 flux maxima by 6 months (figure 27). Thus, when defined by the JMA index, ENSO warm events come before minimum model CO_2 flux, and ENSO cold events come before maximum model CO_2 flux.

Meyers and O'Brien [1995] noted that defining ENSO by SST does not

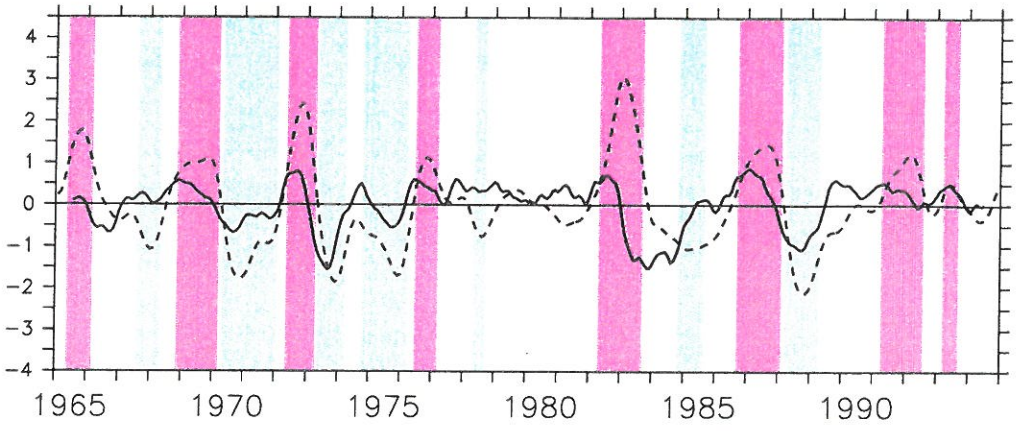


Figure 27: Time series of the JMA index (solid line) and model Q_{CO_2} anomaly (dashed line). Values from both sources have been normalized for comparison. ENSO warm events (as defined by the JMA index) are shown by red bars, ENSO cold events are shown by blue bars.

account for what causes an ENSO warm or cold event. Namely, a large downwelling (upwelling) Kelvin wave that displaces the thermocline in the eastern Pacific upwards (downwards). This displacement decreases (increases) upwelling to the upper layer leading to positive (negative) SST anomalies, and also anomalously low (high) surface values of C_T. In view of this, Meyers and O'Brien have defined a new ENSO index based on sea level change (a proxy for thermocline displacement) at the Galapagos Islands.

Comparing the sea level data at the Galapagos Islands (long. 90°W) from 1965 to 1994 (also at Kapingamarangi from 1979 to 1994 and at Nauru from 1976 to 1994, longitudes 155°E and 167°E respectively) to CO_2 flux from the model gives similar correlation coefficients to the JMA comparison, with smaller lag times for the islands in the west (table 4; figure 28). The length of the sea level time series is different for each island.

The positive maximum correlation coefficients and positive lags at Kapinga-

Table 4: Summary of correlations between island sea level anomaly data and model carbon flux anomaly data.

Island Name	Longitude	Max. R	Lag (months)
Kapingamarangi	155°E	0.51	2
Nauru	167°E	0.45	1
Galapagos	90°W	-0.46	7

marangi and Nauru (islands located in the west) show that sea level rise (thermocline deepening) precedes maximum CO_2 flux by 1 to 2 months, and that sea level drop (thermocline shallowing) predates minimum CO_2 flux by 1 to 2 months. While in the far east, the negative maximum correlation coefficient at Galapagos indicates that sea level rise (thermocline deepening) occurs prior to the minimum CO_2 flux by 7 months, and sea level drop (thermocline shallowing) precedes maximum CO_2 flux by 7 months. As with the JMA ENSO index, deepening thermocline at Galapagos (ENSO warm event) occurs prior to model CO_2 flux minima while shallowing thermocline (ENSO cold event) precedes model CO_2 flux maxima. The positive correlation coefficient for Kapingamarangi and Nauru (i.e., the reverse of the correlation for Galapagos) is due to their location in the western warm pool region where thermocline rises during an ENSO warm event and drops during an ENSO cold event. This reverse can also be seen in the pattern of ENSO warm and cold events (figure 28). ENSO warm event are associated with a rise in sea level at Galapagos and a drop in sea level at Nauru and Kapingamarangi; the reverse is true during an ENSO cold event.

5.3 Atmospheric proxy measurements

Model Q_{CO_2} was also compared to the time series of atmospheric CO_2 concentration at two locations. Following a method similar to *Martín et al.* [1994], the first derivative of anomaly atmospheric CO_2 concentration is correlated with model CO_2 flux anomaly (table 5; figure 29). The two atmospheric CO_2 time series chosen were from Mauna Loa, Hawaii and from Barrow, Alaska [*Thoning et al.*, 1994]. The anthropogenic trend was removed by a least-squares fit to the estimated anthropogenic emission data [*Marland et al.*, 1994], the annual and semi-annual signal was removed by least squares fitting an annual and semi-annual sinusoid, monthly anomalies were determined, and the first derivative was taken.

Table 5: Summary of correlations between first derivative of atmospheric CO_2 anomaly concentrations and model carbon flux anomaly data.

Station Name	Max. R	Lag (months)
Mauna Loa, HI	-0.49	-3
Barrow, AK	-0.56	-5

The negative maximum correlation coefficient and negative lag at both Mauna Loa and Barrow indicates that model ocean-to-atmosphere CO_2 flux maxima precede decreasing atmospheric CO_2 anomalies by 3 months for Mauna Loa and by 5 months for Barrow. The opposite is true for model CO_2 flux minima. Unlike the results obtained when comparing the JMA index and sea level data with model CO_2 flux, maximum model CO_2 flux (associated with ENSO cold events) precedes atmospheric CO_2 growth minima, while minimum

model CO_2 flux (associated with ENSO warm events) precedes atmospheric CO_2 growth maxima. This apparent contradiction was also found by *Martín et al.* [1994]. At first glance the pattern implies that anomalies in atmospheric CO_2 are closely associated with ENSO, but are not directly linked to ocean-atmosphere CO_2 flux from the equatorial Pacific Ocean.

The normalized time series of atmospheric CO_2 concentration at Mauna Loa and Barrow and the model CO_2 flux are replotted using the onset and duration of ENSO warm and cold events as defined by *Meyers and O'Brien* [1995] (figure 30). As previously discussed, Meyers and O'Brien hypothesize that the physical changes associated with ENSO are linked more closely to thermocline changes (and sea level changes) than to SST changes. At Galapagos these thermocline changes (as measured by sea level changes) happen approximately 2 months prior to the associated SST changes. In the central Pacific, the location of the greatest CO_2 flux and CO_2 flux variability as determined by the model, thermocline changes would occur about 2 months earlier than at Galapagos.

At Mauna Loa (figure 30a), at or just before the onset of an ENSO warm event (1976, 1982, 1986, and 1991) atmospheric CO_2 concentration drops and then rises. During ENSO cold events, the growth of atmospheric CO_2 concentration increases and then decreases. However, the pattern seen in ENSO cold events is not as apparent as that in ENSO warm events, especially during 1985. The pattern of ENSO associated changes of atmospheric CO_2 at Barrow (figure 30b) is similar to the pattern at Mauna Loa, especially for the larger events (e.g., 1982 and 1987).

A likely scenario to explain the behavior of the interannual variability of

atmospheric CO_2 concentration is as follows: preceding an ENSO warm event, the thermocline drops in the central Pacific cutting off the supply of C_T to the mixed layer. Trade winds also slow down and the CO_2 flux from this region is greatly reduced leading to an initial decrease in the atmospheric CO_2 concentration. Prior to the resumption of CO_2 flux from the equatorial Pacific the concentration of atmospheric CO_2 begins to increase, indicating either a decrease in extra-equatorial oceanic uptake of CO_2, or an increase in terrestrial CO_2 outgassing.

The process is reversed during an ENSO cold event. CO_2 flux from the central equatorial Pacific increases, leading to an initial increase in atmospheric CO_2 concentration. Later, increased CO_2 uptake by the oceans or land reduces the atmospheric CO_2 concentration.

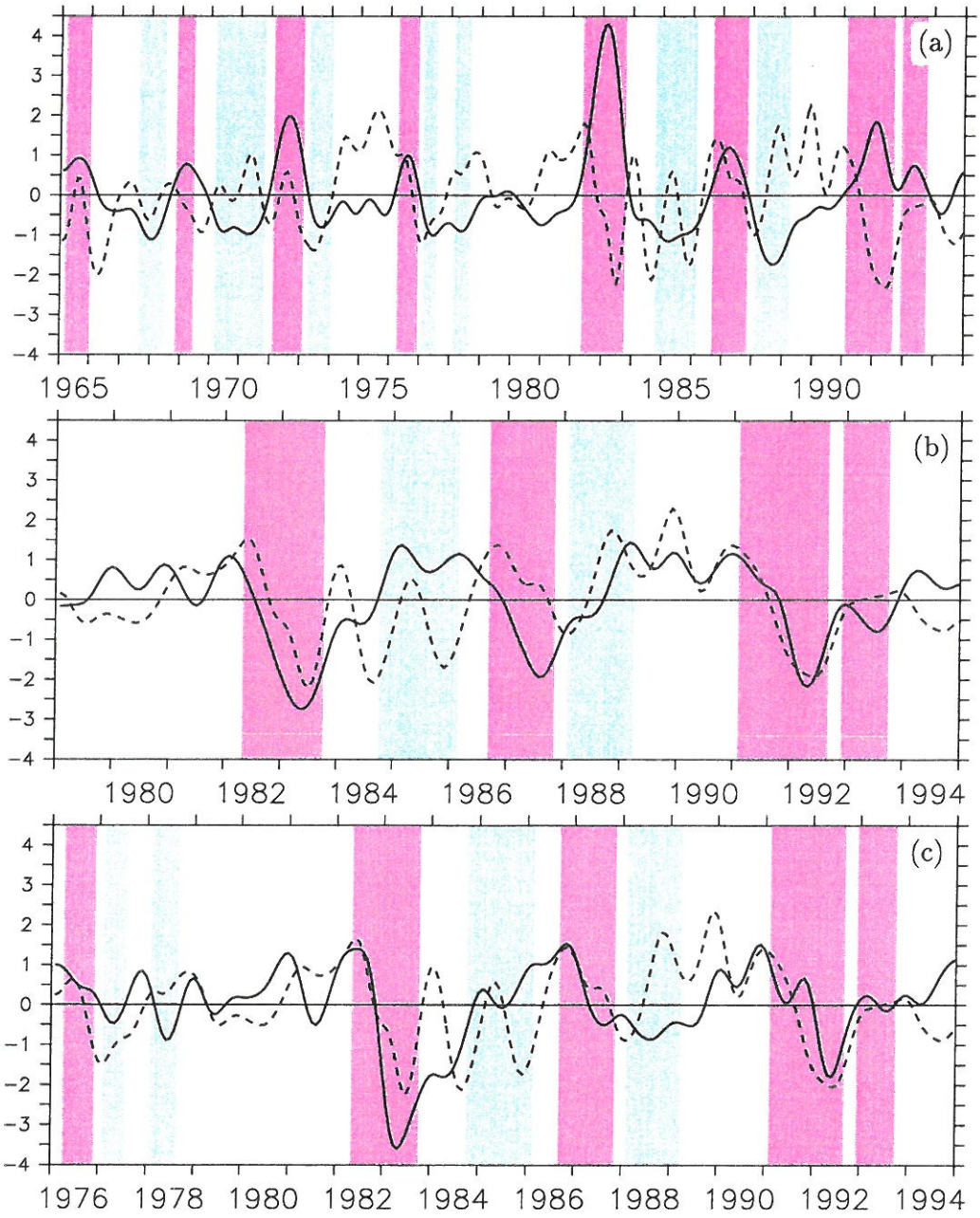


Figure 28: Time series of sea level anomaly (solid line) and model Q_{CO_2} anomaly (dashed line). Values from both sources have been normalized for comparison. ENSO warm events (as defined by sea level at Galapagos [*Meyers and O'Brien*, 1995]) are shown by red bars, ENSO cold events are shown by blue bars. (a) Galapagos (90°19′W, 0°26′S). (b) Kapingamarangi (154°47′E, 1°6′N). (c) Nauru (166°54′E, 0°32′S).

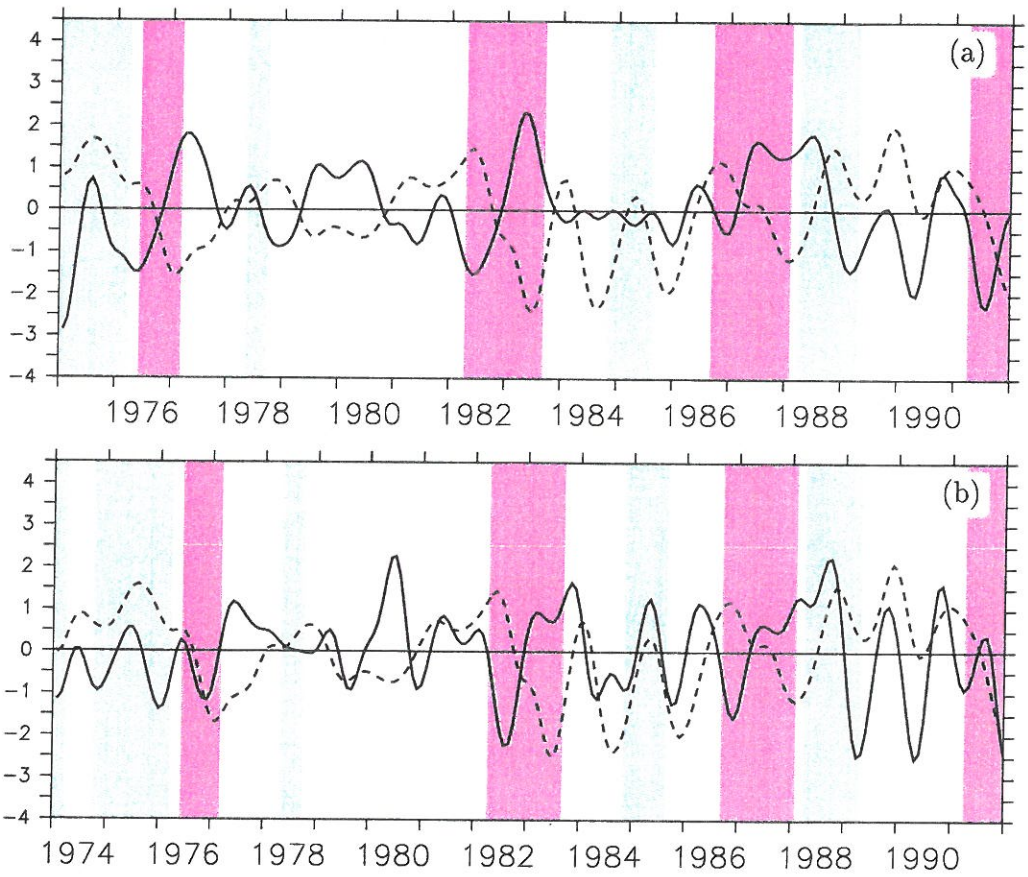


Figure 29: Time series of the first derivative of atmospheric CO_2 concentration anomaly (solid line) and model Q_{CO_2} anomaly (dashed line). Values from both sources have been normalized for comparison. ENSO warm events (as defined by the JMA index) are shown by red bars, ENSO cold events are shown by blue bars. (a) Mauna Loa, Hawaii. (b) Barrow, Alaska.

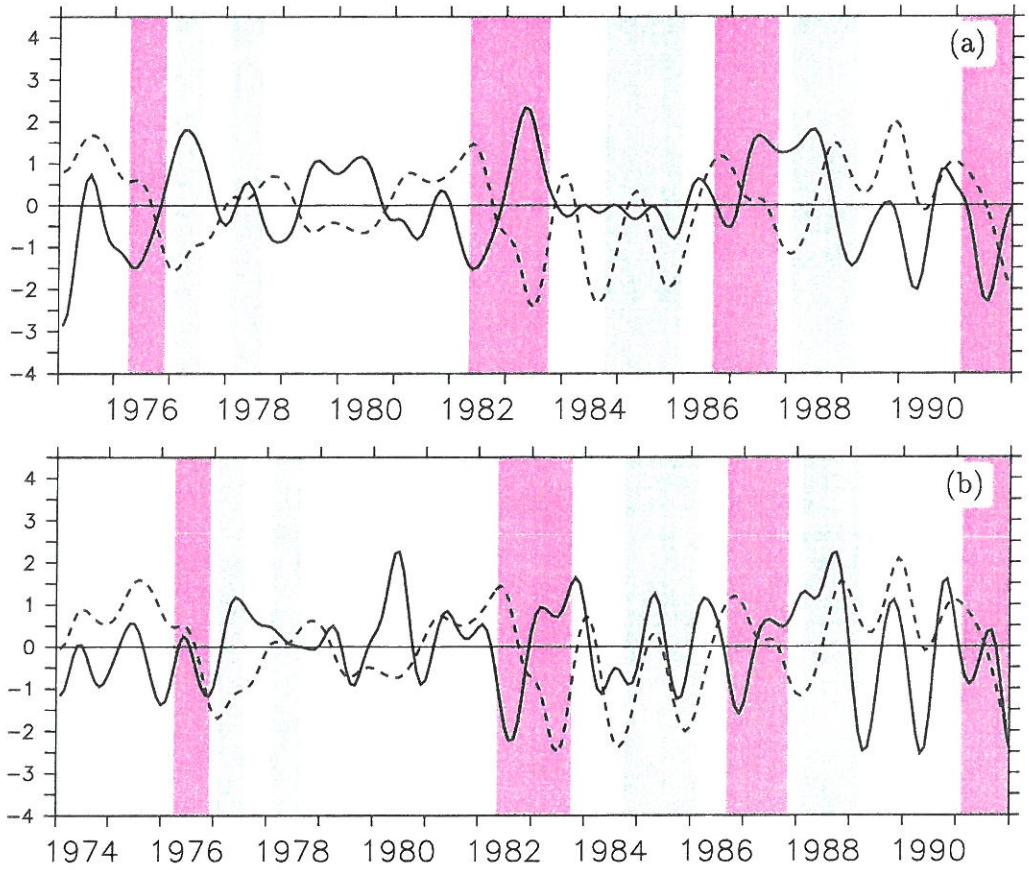


Figure 30: Time series of the first derivative of atmospheric CO_2 concentration anomaly (solid line) and model Q_{CO_2} anomaly (dashed line). Values from both sources have been normalized for comparison. ENSO warm events (as defined by sea level at Galapagos [*Meyers and O'Brien*, 1995]) are shown by red bars, ENSO cold events are shown by blue bars. (a) Mauna Loa, Hawaii. (b) Barrow, Alaska.

6. Discussion

The equatorial Pacific Ocean is the single largest source of ocean-to-atmosphere CO_2 flux. With an estimated annual flux of 1.1 $Gt-C\ yr^{-1}$, and with numerous studies connecting ENSO to large interannual variations in the CO_2 flux and the resulting concentration of atmospheric CO_2, it is important to understand the mechanisms behind the ocean-to-atmosphere CO_2 flux. The conclusions from this work add to the existing knowledge concerning this phenomena. The outcome of the various model experiments detailed in the results section describe the essential physics of the equatorial Pacific mixed layer, and the contributions of the various components, namely, upper layer physics, SST and winds.

The climatologies of anomaly C_T, pCO_2, and Q_{CO_2} (figures 7a-c) indicate that the wind has the most obvious effect. The double high pattern in the wind anomalies (figure 7d) appears as double lows in all the carbon related variables, although the pattern may be shifted somewhat in space and time. Stronger winds increase the CO_2 flux from the ocean to the atmosphere, reducing the C_T in the region and leading to lower pCO_2.

Upwelling (figure 7h) increases the concentration of C_T in the mixed layer. This can be best observed in the high C_T region centered at 180° in the last half of the climatological year following the large upwelling in this region in October. It can also be seen in the low C_T region in the first half of the year centered at 140°W when there is no upwelling. Remnants of these two features (low C_T in the eastern Pacific in the first half of the climatological year and high C_T in the central Pacific in the last half of the year) can also be observed in pCO_2. The climatology of Q_{CO_2} does not retain the high values of C_T and pCO_2 in the

second half of the year, however, the decreased upwelling in the central Pacific in the first half of the year causes a depletion of C_T (and pCO_2) in the surface water greatly reducing the CO_2 flux, despite the strong winds.

SST (figure 7e) has a negligible influence on the climatology of the carbon variables outside of a couple of narrow spatial regions. Even in those regions the effects of SST are small. In the eastern half of the warm pool, a region of the warm pool where there is enough upwelling to refresh the C_T in the surface layer, the high SSTs may help maintain higher pCO_2 values. In addition, in the later part of the climatological year, the cold SSTs in the east reduce the pCO_2 enough so that the double lows in pCO_2 are of about equal magnitude. This is in contrast to the corresponding double low pattern in C_T, where the low C_T in the later part of the year is clearly smaller than the low C_T in the first part of the year. It should also be noted, however, that SST also has some indirect effects (e.g., influencing equatorial winds) that are not accounted for in this study.

Zonal velocity (figure 7f) has a subtle influence on carbon physics. Between 100°W and 80°W there is a constant anomalous eastward zonal velocity (except for the period June to August) which helps maintain high C_T values in the strong coastal upwelling zone. In addition, in the western half of the Pacific there is a pattern of westward then eastward then westward zonal velocity anomalies which appears to influence the high C_T region there.

Meridional velocity (figure 7g) has no apparent effect outside the far western Pacific. The zonally constrained highs in the west are, for the most part, artifacts of islands in the hydrodynamic model caused by setting the biogeochemical

boundaries at ±3°.

The zonal anomaly profiles from the thirty year integration (figures 10a, 11a, and 12a) indicate that the interannual variability occurs mainly in the central Pacific Ocean. C_T, pCO_2, and Q_{CO_2} are high in the easternmost region of the Pacific, but this region is small compared to the width of the entire basin. The western warm pool shows variability in C_T and pCO_2 which is equal to the variability in the central Pacific, but the mean anomalies are much smaller in the western Pacific than in the central Pacific and the Q_{CO_2} is both smaller and less variable in the western Pacific than in the central Pacific.

Results of the thirty year run of the biogeochemical model show a strong link between the model CO_2 flux and ENSO. C_T decreases during an ENSO warm event, and increases during an ENSO cold event (figure 10). The same behavior is seen in pCO_2 (figure 11), i.e., pCO_2 decreases during an ENSO warm event, and increases during an ENSO cold event. However, the correlation between pCO_2 and ENSO is not as high as it is with C_T, and in some of the events the average pCO_2 does not follow this pattern. Q_{CO_2} follows the ENSO cycle more closely than does pCO_2 but not as closely as C_T. In addition, during some of the longer ENSO events anomalously high or low Q_{CO_2} begins to return towards normal before the end of the event.

The input forcing fields explain the patterns in the thirty year run (figures 8 −9). The anomalously low C_T in the western Pacific warm pool is the result of the small upwelling in this region. Without the upwelling, C_T is not replenished in the surface waters. For the same reason pCO_2 in this region is small even though SSTs are higher. CO_2 flux is also low in this region, both because of

low pCO_2 and because of anomalously low wind speeds. The eastern pacific has high values of C_T, pCO_2, and Q_{CO_2} for the same reasons as described in the results section for the climatologies, i.e., strong coastal upwelling and a small but steady eastward current.

C_T in the central Pacific is high in the western half as compared to the eastern half. This pattern is the result of the zonal velocities. The whole region has reasonable upwelling, but zonal velocity is anomalously high (velocity is positive eastward) from 145°E to 170°E, anomalously low from 170°E to 150°W and anomalously high again from 150°W to 100°W. This causes enhanced C_T concentration from 160°E to 160°W and depleted C_T concentration from 160°W to 110°W.

The profile for pCO_2 is similar to that for C_T except that there is an enhanced difference in the central Pacific between the west and the east. This difference is due to higher SST in the west. The pattern of anomalously high pCO_2 in the west and anomalously low pCO_2 in the east is spread out towards the boundaries for the same reason.

The profile of Q_{CO_2} is significantly different from those of C_T and pCO_2, due to the influence of the winds on Q_{CO_2}. The anomalously low winds in the western warm pool magnify the effects of the low pCO_2 in this region resulting in negligible CO_2 flux. However, because higher wind speeds over the eastern half of the central Pacific compensate for the low pCO_2 values in that region, there is a large amount of CO_2 flux between 170°E to 110°W.

Based upon the above observations, a picture of the processes behind the interannual variability can be constructed. During an ENSO warm event the

upwelling decreases, depleting the C_T in the surface waters. This causes a reduction in pCO_2, which is somewhat mitigated by the higher SSTs during a warm event. Wind speeds also become anomalously low during a warm event causing significantly reduced CO_2 flux. CO_2 flux may increase before the end of the warm event if the wind speeds return to normal as they do during some of the longer events.

The reverse happens during an ENSO cold event. Increased upwelling leads to higher C_T concentrations in the surface waters and therefore higher values of pCO_2 (with the colder SSTs making the change in pCO_2 less intense). Equatorial trade winds become stronger and CO_2 flux becomes anomalously high. As during an ENSO warm event, the trade winds may return to normal before the cold event ends causing a decrease in CO_2 flux.

The results of the model run comparisons make evident the relative importance of the various components (upper layer physics, SST, and winds) to the variability of the model produced CO_2 flux. SST has the smallest effect on the interannual variability in the CO_2 flux (figures 16 – 18). Forcing the model with climatological SSTs causes a maximum change of 5% in the CO_2 flux produced from the basic model run. SSTs in the climatological SST run are colder (warmer) during an ENSO warm event (cold event), this causes the pCO_2, and therefore the Q_{CO_2}, to be smaller (larger) compared to the basic model run.

Upper layer physics has an important influence on the interannual variability of CO_2 flux. The box model results (figures 13 – 15) confirm that the physics must be properly resolved to accurately model the CO_2 flux variability. The box model underestimated CO_2 flux by an average of 6%. Moreover, even if

this offset is accounted for, the box model differs from the basic model run by $\pm 10\%$ from this offset.

C_T in the climatological physics run (figure 22) shows none of the interannual variability observed in the basic model run, and there is a large mean difference in both pCO_2 and Q_{CO_2} (figures 23 – 24). The strong influence of the winds on the CO_2 flux is apparent in the time series of Q_{CO_2}. The interannual variability that is not present in the time series of C_T, is plainly visible in the time series of Q_{CO_2}.

The great influence of the winds can also be observed in the climatological wind run (figures 19 – 21). While the winds appear to have little effect on C_T and pCO_2, Q_{CO_2} appears to be highly affected by the winds as evidenced by the difference between the climatological wind run and the basic model run. While there is no mean offset as is the case with the box model run and the climatological physics run, the range of the relative difference in Q_{CO_2} is large.

The biogeochemical model is in good agreement with what little observational evidence exists. The time series of model and observational C_T, pCO_2, and Q_{CO_2} show the same general pattern during ENSO warm and cold events and the neutral years between them. This supports the hypothesis that CO_2 flux from the equatorial Pacific is decreased during an ENSO warm event, and enhanced during an ENSO cold event.

The connection between the variability of the CO_2 flux and ENSO is also validated by the correlation of the proxy ocean variables of SST (JMA index) and sea surface height (island sea level records). The increased SST and upper layer thickness associated with an ENSO warm event causes decreased CO_2 flux,

while the decreased SST and upper layer thickness associated with an ENSO cold event causes increased CO_2 flux.

The inverse relation between the interannual anomaly of atmospheric CO_2 concentration at Mauna Loa and Barrow, and the model CO_2 flux anomaly appears to be contradictory. *Martín et al.* [1994] also found an inverse relationship between ENSO (as determined by SSTs off the coast of Peru) and the growth of atmospheric anomalies at several locations. They suggest that this difference is probably due to changes in the biosphere associated with ENSO, in addition to some unspecified changes in atmospheric and oceanic circulations.

When the interannual variability of atmospheric CO_2 is examined with the onset and duration of ENSO events based on sea level, a different pattern emerges. ENSO warm events are still associated with increased atmospheric CO_2 concentration and ENSO cold events with decreased atmospheric CO_2 concentration. However, atmospheric CO_2 concentration first drops at or just before the onset of an ENSO warm event, and rises at or just before the onset of an ENSO cold event. This initial change is likely due to changes in the CO_2 flux from the central equatorial Pacific, where the changes associated with ENSO happen several months prior to the official beginning of an ENSO event.

The later reversal (increased atmospheric CO_2 concentration during an ENSO warm event, decreased atmospheric CO_2 concentration during an ENSO cold event) are probably due to changes in extra-equatorial oceanic or terrestrial CO_2 flux. A general increase in atmospheric CO_2 concentration during an ENSO warm event (a time when the CO_2 flux from the equatorial Pacific is greatly reduced) must be caused either by increased terrestrial input (possibly

because of a large reduction in flora) or decreased uptake in the oceanic carbon sink regions. Because this study is limited to the equatorial Pacific, a determination of whether there is a large decrease in oceanic uptake during an ENSO warm event is beyond its scope.

The theory of increased terrestrial input is problematic because ENSO warm events are not simply associated with decreased precipitation but also with increased precipitation. For example, a study of ENSO effects on temperature and precipitation in the United States [*Sittel*, 1994] shows that in many areas of the United States increased precipitation is associated with an ENSO warm event.

The results of this research confirm that an accurate representation of the physics, as well as the incorporation of the relevant spatial scales, is required to accurately model the carbon cycle in the surface waters of the equatorial Pacific - the major oceanic source of atmospheric CO_2. Because interannual variations in the CO_2 flux are closely associated with ENSO, realistic simulations are required.

This model is limited in answering the larger question of interannual variations in atmospheric CO_2 concentration. Future work should include modeling a larger portion of the Pacific Basin. This will introduce many new considerations. For example, even though the model used in this study incorporates biological effects, the effects were minimal compared to the other processes driving the CO_2 flux. However, outside of the upwelling rich, constant outgassing equatorial Pacific, biological considerations increase in their importance in determining the uptake of CO_2 into the oceans.

Appendix A. Derivation of Biogeochemical model

Some notational definitions and assumptions used in this chapter:

$$
\begin{aligned}
C &= \text{upper layer } C_T \text{ concentration} \\
C_d \equiv C_{-H} &= \text{upwelled } C_T \text{ concentration} \\
\mathbf{u} &= (u, v); \text{ upper layer velocity vector} \\
w &= \text{vertical velocity (positive upward)} \\
w_d \equiv w_{-H} &= \text{vertical velocity at mixed layer interface} \\
S &= C_T \text{ sources and sinks} \\
H &= \text{upper layer thickness} \\
L &= \text{latitudinal width of model domain} \\
\frac{\partial(\mathbf{u}, C, S, H)}{\partial z} &= 0 \\
\frac{\partial H}{\partial t}, \frac{\partial H}{\partial x}, \frac{\partial H}{\partial y} &= 0 \\
\frac{\partial C_d}{\partial y} &= 0 \\
w_0 &= 0; \text{ no w at sea surface}
\end{aligned}
$$

The tracer conservation equation is:

$$\frac{\partial C}{\partial t} + \nabla \cdot C\mathbf{u} + \frac{\partial Cw}{\partial z} = S. \tag{A1}$$

The sources and sinks in this model include chemical transformation, CO_2 flux to the atmosphere, and biological uptake. The domain of the biogeochemical model is from 3°S to 3°N, and from the bottom of a mixed layer (assumed to be constant) to the sea surface (figure 31).

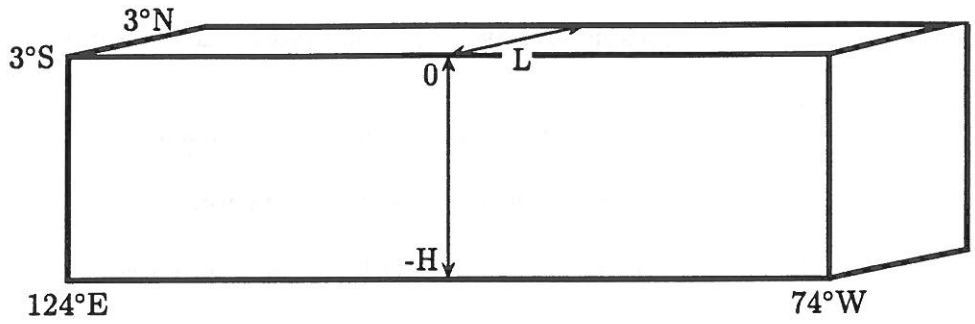


Figure 31: Domain of biogeochemical model.

Integrate equation A1 vertically from $-H$ to 0:

$$\int_{-H}^{0} \frac{\partial C}{\partial t} dz + \int_{-H}^{0} \nabla \cdot \mathbf{u} C dz + \int_{-H}^{0} \frac{\partial Cw}{\partial z} dz = \int_{-H}^{0} S dz \tag{A2}$$

$$\frac{\partial}{\partial t} \int_{-H}^{0} C dz + \nabla \cdot \int_{-H}^{0} C \mathbf{u} dz + Cw \Big|_{-H}^{0} = HS \tag{A3}$$

$$\frac{\partial HC}{\partial t} + \nabla \cdot HC\mathbf{u} + Cw \Big|_{-H}^{0} = HS \tag{A4}$$

$$\frac{\partial HC}{\partial t} + \nabla \cdot HC\mathbf{u} + C_d w_d = HS \tag{A5}$$

Reynolds average (spatial) equation A5 from a fixed southern boundary to a fixed northern boundary, where

$$\overline{(\,)} = \frac{1}{L} \int_{S}^{N} (\,) dy,$$

$$\int_{S}^{N} \frac{\partial HC}{\partial t} dy + \int_{S}^{N} \nabla \cdot HC\mathbf{u} dy + \int_{S}^{N} C_d w_d dy = \int_{S}^{N} HS dy \tag{A6}$$

$$\int_{S}^{N} \frac{\partial HC}{\partial t} dy + \int_{S}^{N} \frac{\partial HCu}{\partial x} dy + \int_{S}^{N} \frac{\partial HCv}{\partial y} dy + \int_{S}^{N} C_d w_d dy = \int_{S}^{N} HS dy \tag{A7}$$

$$\frac{\partial}{\partial t}\int_S^N HCdy + \frac{\partial}{\partial x}\int_S^N HCudy \; + \; HCv\Big|_S^N + \; L\overline{C_d w_d} = L\overline{HS} \tag{A8}$$

$$L\frac{\partial \overline{HC}}{\partial t} + L\frac{\partial \overline{HCu}}{\partial x} + HCv\Big|_S^N + L\overline{C_d w_d} = L\overline{HS} \tag{A9}$$

Since C_d and H are independent of y (thus $\bar{C}_d \equiv C_d$ and $\bar{H} \equiv H$), equation A9 can be rewritten

$$L\frac{\partial H\bar{C}}{\partial t} + L\frac{\partial H\overline{Cu}}{\partial x} + HCv\Big|_S^N + LC_d\bar{w}_d = LH\bar{S}, \tag{A10}$$

and since H is also independent of t and x, divide through by H and L and rearrange equation A10

$$\frac{\partial \bar{C}}{\partial t} + \frac{\partial \bar{C}\bar{u}}{\partial x} + \frac{\partial \overline{C'u'}}{\partial x} = \bar{S} - \frac{C_d\bar{w}_d}{H} - \frac{Cv}{L}\Big|_S^N. \tag{A11}$$

Applying the eddy diffusivity assumption to $\overline{C'u'}$ in equation A11 gives

$$\frac{\partial \bar{C}}{\partial t} + \frac{\partial \bar{C}\bar{u}}{\partial x} + \frac{\partial}{\partial x}K(x)\frac{\partial \bar{C}}{\partial x} = \bar{S} - \frac{C_d\bar{w}_d}{H} - \frac{Cv}{L}\Big|_S^N. \tag{A12}$$

Making the final assumption that K is independent of x gives the final form of the model

$$\frac{\partial \bar{C}}{\partial t} + \frac{\partial \bar{C}\bar{u}}{\partial x} + K\frac{\partial^2 \bar{C}}{\partial x^2} = \bar{S} - \frac{C_d\bar{w}_d}{H} - \frac{Cv}{L}\Big|_S^N. \tag{A13}$$

The biological uptake is modeled assuming carbon uptake in the Redfield ratio in a nitrate limited environment. There is evidence that the equatorial Pacific Ocean is iron limited [*Falkowski*, 1995; *Falkowski and Kolber*, 1995; *Lindley et al.*, 1995; *Takeda and Obata*, 1995], and thus any biological model based on nitrate limitation would be incorrect.

Other researchers have found a strong correlation between upwelling volume and primary productivity *Coale et al.* [1996]; *Murray et al.* [1995], and in

particular a significant decrease in productivity during an ENSO warm event, a period of greatly reduced upwelling [*Landry et al.*, 1995]. If the equatorial Pacific is iron limited than it is likely that the majority of the iron is upwelled and not the result of atmospheric deposition. Assuming that upwelled iron and nitrate remain at a constant concentration, then the nitrate limited model still applies. This is because any new nitrate that is upwelled along with new iron will be taken up by biological production.

Appendix B. Computation of pCO_2 in seawater

The calculation of pCO_2 is based on *Broecker and Takahashi* [1978]

$$pCO_2 = \frac{2C_T - [A]}{K0(2 + K1/a_H)} \tag{B1}$$

$$[A] = [TA] - \frac{K_B[B]}{K_B + a_H} \tag{B2}$$

$$\frac{[A]}{C_T}\left(\frac{a_H}{K_1}\right)^2 + \left(\frac{[A]}{C_T} - 1\right)\frac{a_H}{K_1} + \frac{K_2}{K_1}\left(\frac{[A]}{C_T} - 2\right) = 0 \tag{B3}$$

where pCO_2 is the partial pressure of CO_2; C_T is the concentration of total carbon; [A] is the carbonate alkalinity; K_0 is the solubility of CO_2 in seawater at standard pressure; K_1 and K_2 are the first and second apparent dissociation constants of carbonic acid in seawater; a_H is the hydrogen ion activity; [TA] is the total alkalinity; K_B is the apparent dissociation constant of boric acid in seawater; and [B] is the concentration of borate.

K_0, K_1, K_2, and K_B are empirically determined functions of temperature (K) and salinity (‰), except K_B which is a function of temperature (°C) and Chlorinity (‰)

$$\begin{aligned}\ln(K_0) &= -60.2409 + 93.4517\left(\frac{T}{100}\right) + 23.3585\ln\left(\frac{T}{100}\right) + \\ &\quad S\left[0.023517 - 0.023656\left(\frac{T}{100}\right) + 0.0047036\left(\frac{T}{100}\right)^2\right] \qquad \text{(B4)}\end{aligned}$$

(B5)

$$pK_1 = \frac{812.27}{T} + 3.356 - 0.00171S\ln(T) + 0.000091S^2 \tag{B6}$$

$$pK_2 = \frac{1450.87}{T} + 4.604 - 0.00385S\ln(T) + 0.000182S^2 \tag{B7}$$

$$pK_B = 9.26 - 0.016Cl - 0.010T \tag{B8}$$

where

$$\mathrm{Cl} = \frac{S}{1.80655}.$$

The equation for K_0 is from *Weiss* [1974], equations K_1 and K_2 are from *Goyet and Poisson* [1989], and K_B is from *Li et al.* [1969]. Borate concentration is proportional to salinity [*Culkin*, 1965], and is calculated by

$$[\mathrm{B}] = 4.106 \times 10^{-4} \frac{S}{35}.$$

Hydrogen activity, a_H, is related to pH as follows [*Culberson and Pytkowicz*, 1973]

$$[\mathrm{H}^+] = \frac{a_H}{f_H}$$

$$\mathrm{pH} = -\log[\mathrm{H}^+]$$

where f_H is the total activity coefficient for hydrogen, and $[H^+]$ is the hydrogen ion concentration.

The variations in salinity and titration alkalinity are assumed to be small, and representative values for the equatorial Pacific are chosen. From the Leetmaa Pacific Ocean Analysis Data [*Ji et al.*, 1995, WWW document http://www.cdc.noaa.gov/cdc/data.leetmaa.html] the mean value for surface salinity is 34.551‰. The alkalinity value of 2320 μeq kg^{-1} is from the Geochemical Ocean Sections Study (GEOSECS) data set [*Broecker et al.*, 1982].

Using equations B1 – B3, pCO_2 can be calculated for a particular C_T and temperature (figure 32).

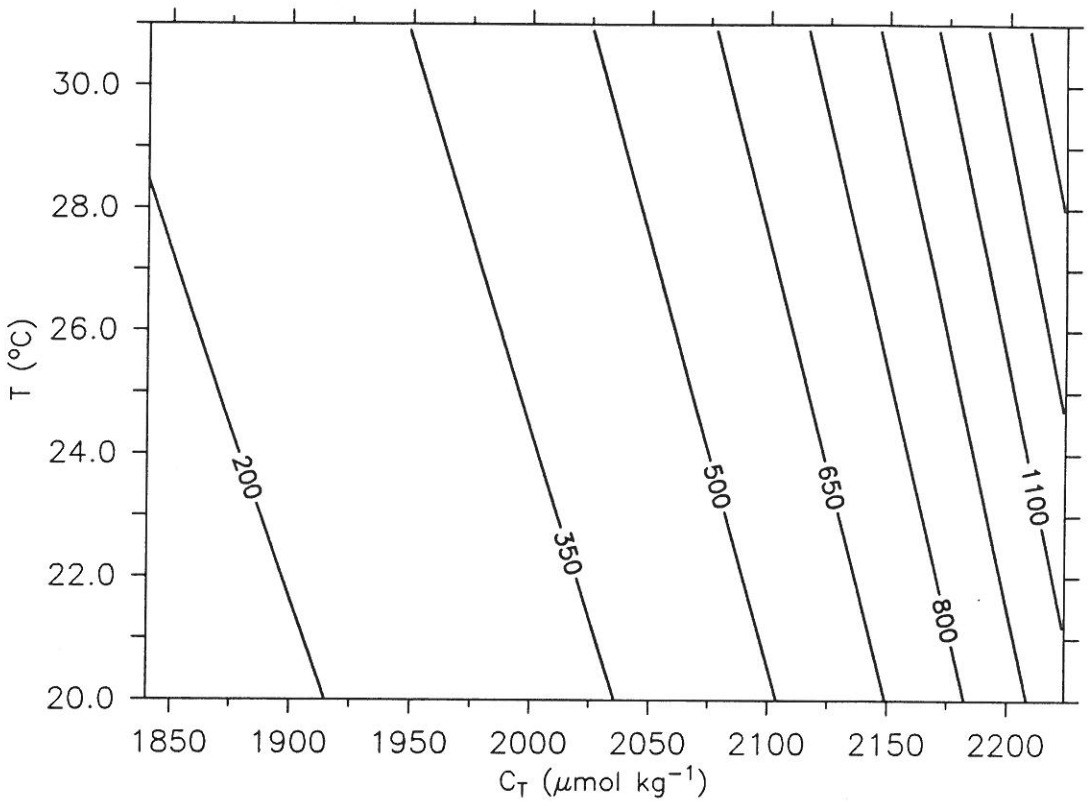


Figure 32: Partial pressure of CO_2 as a function of total carbon (C_T) and temperature (T). Calculated from equations B1– B3. Salinity, S, and titration alkalinity, [TA], are assumed constant (34.551‰, 2320 μeq kg^{-1}).

ACKNOWLEDGEMENTS

The basic support of COAPS is from the Secretary of the Navy Grant from the Physical Oceanography Group of the Office of Naval Research. The data bases used were developed under grants from the Office of Global Programs, NOAA, OGP and the Physical Oceanography Section of the National Science Foundation.

Mark Verschell was supported under the NRL Graduate Program in Physical Oceanography and Meteorology (N00014-90-5-6008), the DOD ASSERT Fellowship "Assimilation of Data and Sensitivity Analysis Using Adjoint Methods for Ocean Models" (ONR#N00014-93-1-1132), and the DOD Fellowship on "High Performance Computing in Physical Oceanography and Meteorology" (ONR Grant No. N00014-85-J-1240).

REFERENCES

Antoine, D., and A. Morel, Modelling the seasonal course of the upper ocean pCO_2 (II). Validation of the model and sensitivity studies, *Tellus*, *47B*, 122–144, 1995.

Broecker, W. S., and E. A. Olson, Radiocarbon from nuclear tests, *Science*, *132*, 712–721, 1960.

Broecker, W. S., and T. Takahashi, The relationship between lysocline depth and in situ carbonate ion concentration, *Deep-Sea Res.*, *25*, 66–95, 1978.

Broecker, W. S., D. W. Spencer, and H. Craig, *GEOSECS Pacific Expedition. Vol. 3, Hydrographic Data 1973-1974*, National Science Foundation, Washington, D. C., 137 pp., 1982.

Camerlengo, A. L., and J. J. O'Brien, Open boundary conditions in rotating fluids, *J. Comput. Phys.*, *35*, 12–35, 1980.

Ciais, P., P. P. Tans, J. W. C. White, M. Trolier, R. J. Francey, J. A. Berry, D. R. Randall, P. J. Sellers, J. G. Collatz, and D. S. Schimel, Partitioning of ocean and land uptake of CO_2 as inferred by $\delta^{13}C$ measurements from the NOAA Climate Monitoring and Diagnostics Laboratory Global Air Sampling Network, *J. Geophys. Res.*, *100*, 5051–5070, 1995.

Coale, K. H., S. E. Fitzwater, R. M. Gordon, K. S. Johnson, and R. T. Barber, Control of community growth and export production by upwelled iron in the equatorial Pacific-Ocean, *Nature*, *379*, 621–624, 1996.

Courant, R., K. Friedrichs, and H. Lewy, On the partial difference equations of mathematical physics, *IBM Journal of Research and Development*, *11*, 215–234, 1967.

Craig, H. D., The natural distribution of radiocarbon and the exchange time of carbon dioxide between atmosphere and sea, *Tellus*, *9*, 1–17, 1957.

Craig, S. G., and K. J. Holmen, Uncertainties in future CO_2 projections, *Global Biogeochem. Cy.*, *9*, 139–152, 1995.

Culberson, C. H., and R. M. Pytkowicz, Ionization of water in seawater, *Mar. Chem.*, *1*, 403–417, 1973.

Culkin, F., The major constituents of sea water., in *Chemical Oceanography, Vol. 1*, edited by J. P. Riley and G. Skirrow, chapter 4, pp. 121–161, Academic Press, London, 1965.

Dandonneau, Y., Sea-surface partial pressure of carbon dioxide in the eastern equatorial Pacific (August 1991 to October 1992): A multivariate analysis of physical and biological factors, *Deep-Sea Res. II, 42*, 349–364, 1995.

Falkowski, P. G., Ironing out what controls primary production in the nutrient-rich waters of the open-ocean, *Global Change Biology, 1*, 161–163, 1995.

Falkowski, P. G., and Z. Kolber, Variations in chlorophyll fluorescence yields in phytoplankton in the world oceans, *Aust. J. Plant Physiol., 22*, 341–355, 1995.

Feely, R. A., R. H. Gammon, B. A. Taft, P. E. Pullen, L. S. Waterman, T. J. Conway, J. F. Gendron, and D. P. Wisegarver, Distribution of chemical tracers in the eastern equatorial Pacific during and after the 1982-1983 El Niño/Southern Oscillation event, *J. Geophys. Res., 92*, 6545–6558, 1987.

Feely, R. A., R. Wanninkhof, C. E. Cosca, P. P. Murphy, M. F. Lamb, and M. D. Steckley, CO_2 distributions in the equatorial Pacific during the 1991-1992 ENSO event, *Deep-Sea Res. II, 42*, 365–386, 1995.

Francey, R. J., P. P. Tans, C. E. Allison, I. G. Enting, J. W. C. White, and M. Trolier, Changes in oceanic and terrestrial carbon uptake since 1982, *Nature, 373*, 326–330, 1995.

Goyet, C., and A. Poisson, New determination of carbonic acid dissociation constants in seawater as a function of temperature and salinity, *Deep-Sea Res., 36*, 1635–1654, 1989.

Hudson, R. J. M., S. A. Gherini, and R. A. Goldstein, Modeling the global carbon cycle nitrogen fertilization of the terrestrial biosphere and the "missing" CO_2 sink, *Global Biogeochem. Cy., 8*, 307–333, 1994.

Inoue, H. Y., and Y. Sugimura, Variations and distributions of CO_2 in and over the equatorial Pacific during the period from the 1986/88 El Niño event to the 1988/89 La Niña event, *Tellus, 44B*, 1–22, 1992.

Inoue, H. Y., M. Ishii, H. Matsueda, M. Ahoyama, and I. Asanuma, Changes in longitudinal distribution of the partial pressure of CO_2 (pCO_2) in the central and western equatorial Pacific, west of 160°W, *Geophys. Res. Lett., 23*, 1781–1784, 1996.

Japan Meteorological Agency, Climate charts of sea surface temperatures of the western north pacific and the global ocean, Marine Department, Japan Meteorological Agency, Tokyo, Japan, 51 pp., 1991.

Ji, M., A. Leetmaa, and J. Derber, An ocean analysis system for seasonal to interannual climate studies, *Mon. Weather Rev.*, *123*, 460–481, 1995.

Kamachi, M., and J. J. O'Brien, Continuous data assimilation of drifting buoy trajectory into an equatorial Pacific Ocean model, *J. Mar. Sys.*, *6*, 159–178, 1995.

Keeling, C. D., The concentration and isotopic abundances of the carbon isotopes, *Geochim. Cosmochim. Ac.*, *13*, 322–334, 1958.

Keeling, C. D., and R. Revelle, Effects of El Nino/Southern Oscillation on the atmospheric content of carbon dioxide, *Meteoritics*, *20(2)*, 437–450, 1985.

Keeling, C. D., R. B. Bacastow, A. F. Carter, S. C. Piper, T. P. Whorf, M. Heimann, W. G. Mook, and H. Roeloffzen, A three-dimensional model of atmospheric CO_2 transport based on observed winds: 1. Analysis of observational data, in *Aspects of Climate Variability in the Pacific and the Western Americas*, edited by D. H. Peterson, pp. 165–236, American Geophysical Union, Washington, D.C., 1989.

Keeling, C. D., T. P. Whorf, M. Whalen, and J. van der Plicht, Interannual extremes in the rate of rise of atmospheric carbon dioxide since 1980, *Nature*, *375*, 666–670, 1995.

Keeling, C. D., and T. P. Whorf, Atmospheric CO_2 records from sites in the SIO air sampling network, in *Trends '93 : A Compendium of Data on Global Change*, edited by T. A. Boden, D. P. Kaiser, R. J. Sepanski, and F. W. Stoss, pp. 16–23. ORNL/CDIAC–65, Carbon Dioxide Information Analysis Center, Oak Ridge National Laboratory, Oak Ridge, Tenn., U.S.A, 1994.

Keller, A. A., and R. A. Goldstein, Oceanic transport and storage of carbon emissions, *Clim. Change*, *30*, 367–395, 1995.

Klepper, O., B. J. de Haan, and H. van Huet, Biochemical feedbacks in the oceanic carbon cycle, *Ecol. Model.*, *75*, 459–469, 1994.

Klepper, O., and B. J. de Haan, A sensitivity study of the effect of global change on ocean carbon uptake, *Tellus*, *47B*, 490–500, 1995.

Landry, M. R., J. Constantinou, and J. Kirshtein, Microzooplankton grazing in the central equatorial Pacific during February and August, 1992, *Deep-Sea Res. II*, *42*, 657–671, 1995.

Li, Y.-H., T. Takahashi, and W. S. Broecker, Degree of saturation of $CaCO_3$ in the oceans, *J. Geophys. Res.*, *74*, 5507–5525, 1969.

Libes, S. M., *An Introduction to Marine Biogeochemistry*, 461–465, John Wiley and Sons, Inc., New York, 1st edition, 734 pp., 1992.

Lindley, S. T., R. R. Bidigare, and R. T. Barber, Phytoplankton photosynthesis parameters along 140°W in the equatorial Pacific, *Deep-Sea Res. II*, *42*, 441–463, 1995.

Maier-Reimer, E., Geochemical cycles in an ocean general circulation model. Preindustrial tracer distributions, *Global Biogeochem. Cy.*, *7*, 645–677, 1993.

Marland, G., R. J. Andres, and T. A. Boden, Global, regional, and national CO_2 emissions, in *Trends '93 : A Compendium of Data on Global Change*, edited by T. A. Boden, D. P. Kaiser, R. J. Sepanski, and F. W. Stoss, pp. 505–584. ORNL/CDIAC–65, Carbon Dioxide Information Analysis Center, Oak Ridge National Laboratory, Oak Ridge, Tenn., U.S.A, 1994.

Martín, F., F. Valero, and J. A. García-Miguel, On the response of the background atmospheric CO_2 growth rate to the anomalies of the sea-surface temperature in the equatorial Pacific Ocean, *Atmos. Environ.*, *3*, 517–530, 1994.

Merlivat, L., J. Etcheto, and J. Boutin, CO_2 exchange at the air-sea interface: Time and space variability, *Adv. Space Res.*, *11*, (3)77–(3)85, 1991.

Meyers, S. D., and J. J. O'Brien, Pacific Ocean influences atmospheric carbon dioxide, *EOS*, *76*, 533,537, 1995.

Murphy, J. M., Transient response of the Hadley Centre coupled ocean-atmosphere model to increasing carbon dioxide. Part III: Analysis of global-mean response using simple-models, *J. Climate*, *8*, 496–514, 1995.

Murray, R. W., M. Leinen, D. W. Murray, A. C. Mix, and C. W. Knowlton, Terrigenous Fe input and biogenic sedimentation in the glacial and interglacial equatorial Pacific-Ocean, *Global Biogeochem. Cy.*, *9*, 667–684, 1995.

Nefedova, E. I., and A. M. Tarko, The zonal model of carbon dioxide global cycle in the "atmosphere-ocean" system, *Oceanology*, *35*, 11–15, 1995.

Neftel, A., H. Friedli, E. Moor, H. Lötscher, H. Oeschger, U. Siegenthaler, and B. Stauffer, Historical CO_2 record from the Siple Station ice core, in *Trends '93 : A Compendium of Data on Global Change*, edited by T. A. Boden, D. P. Kaiser, R. J. Sepanski, and F. W. Stoss, pp. 11–14. ORNL/CDIAC–65, Carbon Dioxide Information Analysis Center, Oak Ridge National Laboratory, Oak Ridge, Tenn., U.S.A, 1994.

Sarmiento, J. L., J. C. Orr, and U. Siegenthaler, A perturbation simulation of CO_2 uptake in an ocean general circulation model, *J. Geophys. Res.*, *97*, 3621–3645, 1992.

de Saussure, N. T., Mémoire sur les variations de l'acide carbonique atmosphérique, *Ann. Chimie et Physique*, *44*, 5–45, 1830.

Schimel, D., I. G. Enting, M. Heimann, T. M. L. Wigley, D. Raynaud, D. Alves, and U. Siegenthaler, CO_2 and the carbon cycle, in *Climate Change 1994: Radiative Forcing of Climate Change and an Evaluation of the IPCC IS92 Emission Scenarios*, edited by J. T. Houghton, L. G. M. Filho, J. Bruce, H. Lee, B. A. Callander, E. Haites, N. Harris, and K. Maskell, pp. 39–71, Cambridge University Press, Cambridge, UK, 1994.

von Schwind, J. J., *Geophysical Fluid Dynamics for Oceanographers*, Prentice-Hall, Inc., Englewood Cliffs, N.J., 1st edition, 307 pp., 1980.

Sittel, M., Differences in the means of ENSO extremes for maximum temperature and precipitation in the United States, Technical Report 94-2, Florida State University, 50 pp., 1994.

Smith, T. M., R. W. Reynolds, R. E. Livezey, and D. C. Stokes, Reconstruction of historical sea-surface temperatures using empirical orthogonal functions, *J. Climate*, *9*, 1403–1420, 1996.

Stricherz, J. N., J. J. O'Brien, and D. M. Legler, Atlas of Florida State University tropical Pacific winds for TOGA 1966-1985, Florida State University, 275 pp., 1992.

Takahashi, T., The carbon dioxide puzzle, *Oceanus*, *32*, (2), 22–29, 1989.

Takeda, S., and H. Obata, Response of equatorial Pacific phytoplankton to subnanomolar Fe enrichment, *Mar. Chem.*, *50*, 219–227, 1995.

Taylor, N. K., Seasonal uptake of anthropogenic CO_2 in an ocean general circulation model, *Tellus*, *47B*, 145–169, 1995.

Tett, S. F. B., Simulation of El Niño/Southern Oscillation like variability in a global AOGCM and its response to CO_2 increase, *J. Climate*, *8*, 1473–1502, 1995.

Thoning, K. W., P. P. Tans, and L. S. Waterman, Atmospheric CO_2 records from sites in the NOAA/CMDL continuous monitoring network, in *Trends '93 : A Compendium of Data on Global Change*, edited by T. A. Boden, D. P.

Kaiser, R. J. Sepanski, and F. W. Stoss, pp. 28–40. ORNL/CDIAC–65, Carbon Dioxide Information Analysis Center, Oak Ridge National Laboratory, Oak Ridge, Tenn., U.S.A, 1994.

Toggweiler, J. R., Anthropogenic CO_2: The natural carbon cycle reclaims center stage, *Rev. Geophys., Suppl.*, *33*, 1249–1252, 1995.

Toggweiler, J. R., K. Dixon, and K. Bryan, Simulations of radiocarbon in a coarse-resolution world ocean model, 1, Steady state prebomb distributions, *J. Geophys. Res.*, *94*, 8217–8242, 1989*a*.

Toggweiler, J. R., K. Dixon, and K. Bryan, Simulations of radiocarbon in a coarse-resolution world ocean model, 2, Distribution of bomb-produced ^{14}C, *J. Geophys. Res.*, *94*, 8243–8264, 1989*b*.

Volk, T. S., Effect of the equatorial Pacific upwelling on atmospheric CO_2 during the 1982-1983 El Niño, *Global Biogeochem. Cy.*, *3*, 267–279, 1989.

Volk, T., and Z. Liu, Controls of CO_2 sources and sinks in the Earth scale surface ocean: Temperature and nutrients, *Global Biogeochem. Cy.*, *2*, 73–89, 1988.

Waliser, D. E., and C. Gautier, A satellite-derived climatology of the ITCZ, *J. Climate*, *6*, 2162–2174, 1993.

Wanninkhof, R., Relationship between wind speed and gas exchange over the ocean, *J. Geophys. Res.*, *97*, 7373–7381, 1992.

Wanninkhof, R., R. A. Feely, H. Chen, C. Cosca, and P. P. Murphy, Surface water fCO_2 in the eastern equatorial Pacific during the 1992-93 El Niño, *J. Geophys. Res.*, *101*, 16,333–16,343, 1996.

Weiss, R. F., Carbon dioxide in water and seawater: The solubility of non-ideal gas, *Mar. Chem.*, *2*, 203–215, 1974.

Winguth, A. M. E., Windinduzierte Variabilität in der Warmwassersphäre von 1981-1987, Teil II, Fluktuationen im Kohlenstoffkreislauf, *Examensarbeit 14*, Max-Planck-Institut für Meteorologie, Hamburg, Germany, 1992.

Winguth, A. M. E., M. Heimann, K. D. Kurz, E. Maier-Reimer, U. Mikolajewicz, and J. Segschneider, El Niño-Southern Oscillation related fluctuations of the marine carbon cycle, *Global Biogeochem. Cy.*, *8*, 39–63, 1994.

Wong, C. S., Y.-H. Chan, J. S. Page, G. E. Smith, and R. D. Bellegay, Changes in equatorial CO_2 flux and new production estimated from CO_2 and nutrient levels in Pacific surface waters during the 1986/87 El Niño, *Tellus*, *45B*, 64–79, 1993.